TUM School of Engineering and Design

A mortar finite element formulation including viscoelastic layers for component-based vibration analysis

Alexander Paolini

Vollständiger Abdruck der von der TUM School of Engineering and Design der Technischen Universität München zur Erlangung des akademischen Grades eines

Doktors der Ingenieurwissenschaften

genehmigten Dissertation.

Vorsitzender:	Prof. Dr.-Ing. André Borrmann
Prüfer der Dissertation:	
	1. Prof. Dr.rer.nat. Ernst Rank
	2. Prof. Dr.-Ing. habil. Gerhard Müller
	3. Prof. Dr.-Ing. Martin Schanz

Die Dissertation wurde am 18.11.2021 bei der Technischen Universität München eingereicht und durch die TUM School of Engineering and Design am 16.05.2022 angenommen.

Abstract

Finite element vibration analysis of complex structures can require a high effort for modeling and computation. The simulation of structure-borne sound transmission in solid timber buildings is a good example. In this case, not only the parts themselves, such as cross-laminated timber (CLT) panels, but also their connections must be modeled correctly. Volumetric finite elements are well suited to represent the three-dimensional displacement field in such structures. However, the computational costs can be high, for instance, due to excessive mesh refinement at joints. Creating an efficient mesh, on the other hand, can be associated with a large amount of manual work. The modeling effort becomes even more significant if the connections contain thin damping layers to reduce the transmission of structure-borne sound.

This thesis, therefore, proposes a component-based modeling approach. Therein, each structural part is discretized separately by high-order finite elements and weakly coupled using a modified mortar formulation that can represent linear viscoelastic layers in a dimensionally reduced form. This procedure makes it possible to better adapt the discretization of structures to the geometry of each component and to consider the effect of thin damping layers without explicitly resolving them by finite elements. Thus, the generation of computationally efficient volumetric models can be significantly simplified and even automated. The accuracy and efficiency of the proposed approach are moreover demonstrated by various examples, ranging from a two-component CLT assembly to a complete solid timber building.

Additive manufacturing (AM) is investigated in addition to solid timber construction as another application area for the modified mortar method. The use of AM in the construction industry is currently being studied intensively because of its significant potential. It allows building companies to automate the construction process and to produce functionally graded structures with complex geometries. In this part of the present thesis, first, the current state of AM in construction is reviewed with a particular focus on digital planning methods. Based on these insights, a heterogeneous structure exhibiting extraordinary stiffness and damping properties is finally analyzed and designed on multiple scales using advanced numerical methods, including the proposed mortar approach.

Zusammenfassung

Schwingungsanalysen komplexer Strukturen unter Verwendung der Finite-Elemente-Methode können einen hohen Modellierungs- und Rechenaufwand erfordern. Ein gutes Beispiel hierfür ist die Simulation von Körperschallübertragung in Massivholzgebäuden. In diesem Fall müssen nicht nur die Bauteile selbst, wie z. B. Brettsperrholzplatten, sondern auch deren Verbindungen korrekt modelliert werden. Volumenelemente sind gut geeignet, das dreidimensionale Verschiebungsfeld in solchen Strukturen abzubilden. Die Rechnungen können jedoch aufwendig sein, beispielsweise aufgrund von übermäßigen Netzverfeinerungen an Stoßstellen. Wird hingegen ein effizientes Berechnungsnetz erstellt, kann dies mit viel manueller Arbeit verbunden sein. Der Modellierungsaufwand steigt sogar noch weiter an, wenn dünne Dämpfungsschichten zur Reduzierung der Körperschallübertragung in den Bauteilverbindungen eingesetzt werden.

Diese Arbeit stellt deshalb einen bauteilorientierten Modellierungsansatz vor. Darin werden die Bauteile getrennt voneinander mit finiten Elementen hoher Ordnung diskretisiert und in integraler Form miteinander gekoppelt. Hierzu wird eine modifizierte Mortar-Formulierung verwendet, welche die dimensionsreduzierte Abbildung linear viskoelastischer Zwischenschichten erlaubt. Diese Vorgehensweise ermöglicht es, die Diskretisierung von Strukturen besser an die Bauteilgeometrien anzupassen und die Wirkung dünner Dämpfungsschichten zu berücksichtigen, ohne dass diese explizit mit finiten Elementen aufgelöst werden müssen. Die Erstellung effizienter Volumenmodelle kann somit deutlich vereinfacht und sogar automatisiert werden. Darüber hinaus werden die Genauigkeit und die Effizienz des vorgestellten Ansatzes anhand mehrerer Beispiele gezeigt, angefangen bei einem Decken-Wandanschluss aus Brettsperrholz bis hin zu einem gesamten Massivholzgebäude.

Die additive Fertigung wird neben dem Massivholzbau als weiteres Anwendungsgebiet für die modifizierte Mortar-Methode untersucht. Der Einsatz additiver Fertigungsverfahren in der Bauindustrie wird derzeit wegen seines großen Potenzials intensiv erforscht. Bauunternehmen können hierdurch den Bauprozess automatisieren und funktional gradierte Strukturen mit komplexer Geometrie erzeugen. In diesem Teil der vorliegenden Doktorarbeit wird zuerst der aktuelle Forschungsstand zur additiven Fertigung im Bauwesen präsentiert, wobei ein besonderer Schwerpunkt auf digitale Planungsmethoden gelegt wird. Auf der Grundlage dieser Erkenntnisse wird schließlich eine heterogene Struktur, die über außergewöhnliche Steifigkeits- und Dämpfungseigenschaften verfügt, auf verschiedenen Skalenebenen unter Verwendung fortschrittlicher numerischer Methoden, inklusive des vorgestellten Mortar-Ansatzes, analysiert und gestaltet.

Acknowledgments

This thesis resulted from the scientific research I conducted during my employment at the Chair for Computation in Engineering, now Chair of Computational Modeling and Simulation, of the Technical University of Munich from 2015 to 2021. It was made possible by the financial support of the German Research Foundation (DFG) and the Leonhard Obermeyer Center (LOC). I am grateful to everyone who contributed to this work.

In particular, I want to thank my doctoral supervisor Prof. Ernst Rank for his constant support and trust. He provided guidance and advice. Beyond that, he created a productive and collaborative environment where I enjoyed great freedom.

Special thanks are also due to Dr. Stefan Kollmannsberger, who was always there to give advice, to go into the details of a problem, and to discuss new ideas.

I would like to thank my colleagues for the great collaboration and all the fun. It was a huge pleasure to be part of this group.

Moreover, I am grateful to all partners in the project *Vibroakustik im Planungsprozess für Holzbauten* at the Technical University of Munich, Rosenheim University of Applied Sciences, and Getzner Werkstoffe GmbH. They provided data and insights that are an essential foundation for this thesis. Especially, I want to thank Prof. Gerhard Müller. Besides being an important project partner, he sparked my enthusiasm for structural mechanics in the first place during my bachelor and master studies.

Many heartfelt thanks go to my family and friends for their encouragement and unconditional support.

Publications

This thesis is based on the following articles, which were published in peer-reviewed scientific journals. The footnotes [a] [b] [c] [d] [e] serve to reference the original publications and to indicate literal transposition.

Paper A

A high-order finite element model for vibration analysis of cross-laminated timber assemblies.

A. Paolini, S. Kollmannsberger, C. Winter, M. Buchschmid, G. Müller, A. Rabold, S. Mecking, U. Schanda, E. Rank.

Building Acoustics 24(3):135-158, 2017. DOI: 10.1177/1351010X17727126

Abstract: The vibration behavior of cross-laminated timber (CLT) components in the low frequency range can be predicted with high accuracy by the finite element method. However, the modeling of assembled CLT components has been studied only scarcely. The three-dimensional p-version of the finite element method, which is characterized by hierarchic high-order shape functions, is well suited to consider coupling and support conditions. Furthermore, a small number of degrees of freedom can be obtained in the case of thin-walled structures by using p-elements with high aspect ratios and anisotropic ansatz spaces. In this paper, a model for CLT assemblies made of volumetric high-order finite elements is presented. Two representative types of connections are investigated, one with an elastomer between the CLT components and the other without. The model is validated, and suitable ranges for the stiffness parameters of the finite elements which represent the junctions are identified.

Contributions: Alexander Paolini created the finite element models, conducted the numerical study, and wrote the article. Simon Mecking, Andreas Rabold, and Ulrich Schanda provided the results of the experimental tests. Furthermore, they helped to interpret these results together with Christoph Winter, Martin Buchschmidt, and Gerhard Müller. Stefan Kollmannsberger and Ernst Rank supervised this investigation. All authors reviewed the paper and approved the final version.

---

[a] This section, passage, or figure is taken from Paper A in an adjusted version and is reproduced here with the permission of the copyright holder.

[b] This section, passage, figure, or table is taken from Paper B in an adjusted version and is reproduced here with the permission of the copyright holder.

[c] This section, passage, or figure is taken from Paper C in an adjusted version and is reproduced here with the permission of the copyright holder.

[d] This chapter or passage is taken from Paper D in an adjusted version and is reproduced here with the permission of the copyright holder.

[e] This chapter, passage, or figure is taken from Paper E in an adjusted version and is reproduced here with the permission of the copyright holder.

Paper B

A mortar formulation including viscoelastic layers for vibration analysis.
A. Paolini, S. Kollmannsberger, E. Rank, T. Horger, B. Wohlmuth.
Computational Mechanics 63(1):23-33, 2019. DOI: 10.1007/s00466-018-1582-9

Abstract: In order to reduce the transfer of sound and vibrations in structures such as timber buildings, thin elastomer layers can be embedded between their components. The influence of these elastomers on the response of the structures in the low frequency range can be determined accurately by using conforming hexahedral finite elements. Three-dimensional mesh generation, however, is yet a non-trivial task, and mesh refinements which may be necessary at the junctions can cause a high computational effort. One remedy is to mesh the components independently from each other and to couple them using the mortar method. Further, the hexahedral mesh for the thin elastomer layer itself can be avoided by integrating its elastic behavior into the mortar formulation. The present paper extends this mortar formulation to take damping into account such that frequency response analyses can be performed more accurately. Finally, the proposed method is verified by numerical examples.

Contributions: Alexander Paolini included material damping into the mortar formulation for elastomer bedded structures and implemented it in the finite element code. He also created the numerical models, performed the simulations, and wrote the article. Thomas Horger and Barbara Wohlmuth helped to discuss the results. Stefan Kollmannsberger and Ernst Rank supervised this research. All authors reviewed the paper and approved the final version.

Paper C

BIM-based structural dynamic analysis using higher-order volumetric finite elements.
A. Paolini, F. Frischmann, S. Kollmannsberger, A. Rabold, T. Horger, B. Wohlmuth, E. Rank.
Bauingenieur 93(4):160-166, 2018. DOI: 10.37544/0005-6650-2018-04-76

Abstract: Building Information Modeling allows to automate the generation of simulation models and thus forms an important basis for saving time and costs as well as for increasing the quality in the planning of buildings. The type of the simulation model is largely dependent on the specific problem to resolve. For vibration analyses of solid timber constructions, a mechanically correct representation of the junctions between the components is essential. For this purpose, models consisting of hexahedral finite elements are much better suited than shell elements. With available mesh generators, however, matching hexahedral meshes can only be created automatically in the case of specific building geometries and show a large number of elements at joints, which can lead to a high computational effort. Therefore, an alternative procedure to derive a hexahedral Finite Element Model from a Buiding Information Model (BIM) is presented. Therein, the building components defined in the BIM are meshed individually, and

their connections to each other are modeled by means of the mortar method. A great computational efficiency is gained by using higher order shape functions in combination with a relatively coarse mesh. After the description of the procedure, its applicability is demonstrated in the case of a multistory timber building.

Contributions: Alexander Paolini modified the finite element code to solve large eigenproblems, conducted the structural dynamic analysis, and wrote the article. Felix Frischmann developed the code to automatically generate the simulation model from a Building Information Model. Andreas Rabold provided the measurement results and the construction plans. Stefan Kollmannsberger and Ernst Rank supervised this project. All authors reviewed the paper and approved the final version.

Paper D

Additive manufacturing in construction: A review on processes, applications, and digital planning methods.

A. Paolini, S. Kollmannsberger, E. Rank.

Additive Manufacturing 30, 2019. DOI: 10.1016/j.addma.2019.100894

Abstract: The application of additive manufacturing (AM) in construction has been increasingly studied in recent years. Large robotic arm- and gantry-systems have been created to print building parts using aggregate-based materials, metals, or polymers. Significant benefits of AM are the automation of the production process, a high degree of design freedom, and the resulting potential for optimization. However, the building components and 3D printing processes need to be modeled appropriately. In this paper, the current state of AM in construction is reviewed. AM processes and systems as well as their application in research and construction projects are presented. Moreover, digital methods for planning 3D-printed building parts and AM processes are described.

Contributions: Alexander Paolini conducted the study and wrote the article. Stefan Kollmannsberger and Ernst Rank supervised this research. All authors reviewed the paper and approved the final version.

Paper E

Multiscale analysis of high damping composites using the finite cell and the mortar method.

A. Paolini, N. Korshunova, S. Kollmannsberger, E. Rank.

International Journal of Structural Stability and Dynamics 21(11):2150149, 2021.
DOI: 10.1142/S0219455421501492

Abstract: Metal lattice structures filled with a damping material such as polymer can exhibit high stiffness and good damping properties. Mechanical simulations of parts made from these composites can, however, require a large modeling and computational effort

because relevant features such as complex geometries need to be represented on multiple scales. The finite cell method (FCM) and numerical homogenization are potential remedies for this problem. Moreover, if the microstructures are placed in between the components of assemblies for vibration reduction, a modified mortar technique can further increase the efficiency of the complete simulation process. With this method, it is possible to discretize the components separately and to integrate the viscoelastic behavior of the composite damping layer into their weak coupling. The present paper provides a multiscale computational material design framework for such layers, based on FCM and the modified mortar technique. Its efficiency, even in the case of complex microstructures, is demonstrated in numerical studies. Therein, computational homogenization is first performed on various microstructures before the resulting effective material parameters are used in larger-scale simulation models to investigate their effect and to verify the employed methods.

Contributions: Alexander Paolini modified the mortar formulation to represent orthotropic damping layers and implemented this approach in the finite element code. He also created the numerical models, conducted the multiscale investigation, and wrote the article. Nina Korshunova developed the code for computational homogenization. Furthermore, she helped to create the numerical models and to discuss the results. Stefan Kollmannsberger and Ernst Rank supervised this research. All authors reviewed the paper and approved the final version.

Contents

Chapter 1

Introduction

1.1 Motivation

The finite element method (FEM) allows the prediction of sound and vibrations in the low frequency range. It is therefore a powerful design tool to improve the serviceability of buildings, including sound insulation [1]. In order to obtain meaningful results, relevant aspects of the mechanical problem need to be represented properly. A standard approach in structural engineering is to model each building component with dimensionally reduced elements such as beams, plates, or shells. Their main advantages are the relatively low costs of modeling and computation. However, the range of application is limited due to the underlying assumptions on the stresses, strains, and displacements. Volumetric finite elements may be required if the components or their connections exhibit a complex three-dimensional (3D) displacement field. This can be the case, for example, in cross-laminated timber (CLT) assemblies or structures made by additive manufacturing (AM):

- CLT panels comprise layers of wooden boards, which are glued together crosswise. Thus, biaxial load transfer is possible [2]. Besides the particular structure of CLT components, their connections must be modeled correctly in order to calculate the vibration behavior of CLT assemblies.
- AM parts are created by joining materials in layers. In this way, intricate geometries and material distributions can be produced automatically, starting from a digital model. Examples are functionally graded materials and cellular structures [3–5]. Complex structural behavior can arise from both the layerwise production process and a heterogeneous object design.

The modeling and computational effort required for a volumetric finite element analysis can be fortunately reduced by advanced discretization methods. In the p-version of the finite element method (p-FEM), high-order elements are used to get accurate numerical results [6]. Due to their better convergence properties, considerably greater computational efficiency can be achieved in comparison to linear or quadratic elements. However, conforming hexahedral meshes can be created automatically just for specific geometries. Furthermore, strong local refinement may occur at connections between structural components and increase the computational costs significantly. Such modeling difficulties can be overcome by fictitious domain and multidomain methods:

- Fictitious domain methods such as the finite cell method (FCM) do not need a mesh that conforms to the boundary of a domain. It is sufficient to employ a Cartesian grid or an equally simple mesh. Hence, elements may be cut by the boundary. The original domain is, however, restored in these methods during the integration of the element matrices and load vectors [6–8].
- Multidomain approaches such as the mortar and the penalty method allow dividing a structure into weakly coupled subdomains that are discretized separately. Since the meshes are not required to match each other at the interfaces, mesh generation can be simplified and better adapted to the geometry. Moreover, different numerical approaches can be employed for the subdomains [9–11].

Based on numerical vibration analysis, effective design changes can be implemented. A common measure to reduce the transfer of sound and vibrations is to embed thin elastomer layers between the components. Compared to rigid connections, however, junctions including damping layers are more difficult to model and can lead to higher computational costs if conformingly refined meshes are used. Alternative approaches for flexible connections can be found in [12–17]. In [14], for example, springs and dashpots serve as a representation of an elastomer layer in a volumetric FE model of a timber assembly. This method still does not allow for an independent mesh generation of the coupled parts. In contrast, the mesh for each component and elastomer can be created separately by applying the dynamic substructuring technique presented in [16], where interface reductions are performed. A rigid body constraint was chosen for the interface surfaces of the elastomers. This means that the procedure is not necessarily appropriate for viscoelastic layers with large interface surfaces, such as elastomer strips [16]. This limitation does not hold for the mortar formulation developed by Horger et al. [17]. Therein, a Robin-type condition is employed for coupling domains and representing elastic layers between them. The good performance and the stability of the method in combination with the p-version of FEM were also shown in [17]. However, this formulation neglects damping within the intermediate layer because it was only developed for modal analysis. As the loss factor of the layer material is in general much higher than that of other structural materials, it can have a significant influence on the vibration behavior of the entire structure. Hence, for a more realistic model, viscoelasticity needs to be taken into account.[b]

1.2 Objectives

The aim of this work is to develop an accurate and efficient procedure for vibration analysis of structures containing thin damping layers. In the proposed approach, the components are discretized independently from each other with high-order hexahedral finite elements. The subdomains are then weakly coupled by employing a mortar formulation that is able to consider viscoelastic layers in a dimensionally reduced form. Parts with complex structural features and their connections can thus be represented with low modeling and computational effort. After deriving the modified mortar formulation, the accuracy and efficiency of the component-based approach are verified by several examples from two application fields: solid timber construction and additive manufacturing.

The contributions of this thesis are:

- Development and validation of a high-order FE model that efficiently computes the vibrations of CLT assemblies with and without elastomer layers in the low frequency range (Paper A).
- Modification and verification of a mortar formulation to reduce the modeling and computational costs for vibration analysis of structures containing isotropic damping layers – such as elastomer bedded CLT assemblies (Paper B).
- Structural dynamic analysis of a solid timber building that demonstrates the good suitability of the mortar-based approach within the planning process of construction projects (Paper C).
- Review of AM in construction with a particular focus on digital planning methods (Paper D).
- Extension and verification of the modified mortar formulation to represent damping layers made of composite microstructures that can be additively manufactured (Paper E).
- Multiscale analysis of high damping composites to demonstrate the potential of AM and of the proposed mortar-based approach in combination with FCM (Paper E).

1.3 Structure

This thesis is structured as follows. Chapter 2 outlines the fundamentals of the finite element method for linear elastic and viscoelastic problems. Furthermore, techniques to reduce the costs of modeling and computation are described, namely p-FEM, FCM, and the mortar method. In this context, the mortar formulation modified to represent thin damping layers is introduced.

Chapters 3 to 5 summarize Papers A to E and discuss the results. The proposed mortar-based approach is applied here and investigated with respect to its accuracy. In Chapter 3, first, a high-order finite element model of a two-component CLT assembly is validated by measurements using a conforming mesh. Then, mortar-based models of different solid timber structures ranging from the aforementioned CLT assembly to a complete multistory building are presented and studied. This is followed by a description of the second application area: additive manufacturing. Chapter 4 reviews the current state of AM in construction. 3D printing processes and digital planning methods are explained. After that, high damping composites that can be produced by AM are analyzed on multiple scales in Chapter 5 by employing p-FEM, FCM, and the modified mortar method.

Chapter 6 finally provides a concluding discussion with an outlook on future work.

Chapter 2

Numerical methods for vibration analysis

This chapter presents numerical methods to predict structural vibrations. First, the finite element method and its p-version are outlined for linear elastic and viscoelastic problems. The p-version of FEM can yield significant computational savings and serves as a basis for the subsequently described finite cell and mortar methods, which in turn provide a greatly simplified modeling process. Finally, a modified mortar formulation is introduced to further improve the modeling and computational efficiency of vibration analyses for structures that contain thin damping layers.

2.1 The finite element method

2.1.1 Linear elasticity

The displacements $\mathbf{u}$ of a three-dimensional body described in the coordinate system (x, y, z) can be calculated at each time t based on the principle of virtual work. This principle says that, in the state of equilibrium, the total internal work resulting from any compatible variation $\delta\boldsymbol{u}$ of the displacements is equal to the corresponding total external work [18]:

$$\delta W_i = \delta W_e \tag{2.1}$$

with:

$$\delta W_i = \int_\Omega \delta\boldsymbol{\varepsilon}^T \boldsymbol{\sigma}\, d\Omega \tag{2.2}$$

$$\delta W_e = \int_\Omega \delta\mathbf{u}^T \left(\mathbf{b} - \rho\frac{\partial^2\mathbf{u}}{\partial t^2}\right) d\Omega + \int_{\Gamma_t} \delta\mathbf{u}^T\mathbf{t}\, d\Gamma. \tag{2.3}$$

The virtual strains $\delta\boldsymbol{\varepsilon}$, which are associated with $\delta\boldsymbol{u}$, and the stresses $\boldsymbol{\sigma}$ are given in Voigt notation. Furthermore, ρ denotes the density, $\partial^2\mathbf{u}/\partial t^2$ the acceleration, $\mathbf{b}$ the body force within the domain Ω, and $\mathbf{t}$ the traction on Γ_t, as depicted for two dimensions in Figure 2.1. Provided that the displacements $\mathbf{u}$ are small, the strains $\boldsymbol{\varepsilon}$ can be approximated

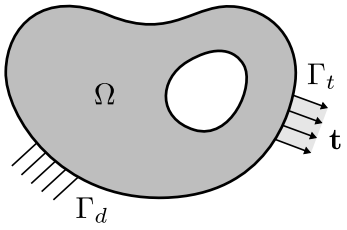

Figure 2.1: Linear elastic body.

by the linear kinematic equation:

$$\boldsymbol{\varepsilon} = \mathbf{D}\mathbf{u} \tag{2.4}$$

where $\mathbf{D}$ is a matrix of first-order partial differential operators:

$$\mathbf{D} = \begin{bmatrix} \frac{\partial}{\partial x} & 0 & 0 & \frac{\partial}{\partial y} & 0 & \frac{\partial}{\partial z} \\ 0 & \frac{\partial}{\partial y} & 0 & \frac{\partial}{\partial x} & \frac{\partial}{\partial z} & 0 \\ 0 & 0 & \frac{\partial}{\partial z} & 0 & \frac{\partial}{\partial y} & \frac{\partial}{\partial x} \end{bmatrix}^T . \tag{2.5}$$

Moreover, a linear relationship between the stresses $\boldsymbol{\sigma}$ and the strains $\boldsymbol{\varepsilon}$ is assumed:

$$\boldsymbol{\sigma} = \mathbf{C}\boldsymbol{\varepsilon}. \tag{2.6}$$

The constitutive matrix $\boldsymbol{C}$ neither depends on the levels of the stresses and strains nor on their development over time. This means that there is no delay between $\boldsymbol{\sigma}$ and $\boldsymbol{\varepsilon}$. The entries of $\boldsymbol{C}$ for orthotropic, cubic, and isotropic materials:

$$\boldsymbol{C} = \begin{bmatrix} C_{11} & C_{12} & C_{13} & 0 & 0 & 0 \\ C_{21} & C_{22} & C_{23} & 0 & 0 & 0 \\ C_{31} & C_{32} & C_{33} & 0 & 0 & 0 \\ 0 & 0 & 0 & C_{44} & 0 & 0 \\ 0 & 0 & 0 & 0 & C_{55} & 0 \\ 0 & 0 & 0 & 0 & 0 & C_{66} \end{bmatrix} \tag{2.7}$$

can be computed from a certain number of independent material parameters [19, 20]:

- **Orthotropic materials**, such as wood, have three orthogonal planes of symmetry. They are characterized by nine parameters, namely three Young's moduli E_1, E_2, E_3, three Poisson's ratios ν_{12}, ν_{23}, ν_{31}, and three shear moduli G_{12}, G_{23}, G_{31}:

$$\begin{aligned} C_{11} &= \frac{E_1}{D_0}\left(1-\nu_{23}^2\frac{E_3}{E_2}\right), \quad C_{12} = \frac{E_1}{D_0}\left(\nu_{12}\frac{E_2}{E_1}+\nu_{23}\nu_{31}\right), \quad C_{44} = G_{12}, \\ C_{22} &= \frac{E_2}{D_0}\left(1-\nu_{31}^2\frac{E_1}{E_3}\right), \quad C_{13} = \frac{E_1}{D_0}\left(\nu_{12}\nu_{23}\frac{E_3}{E_1}+\nu_{31}\right), \quad C_{55} = G_{23}, \\ C_{33} &= \frac{E_3}{D_0}\left(1-\nu_{12}^2\frac{E_2}{E_1}\right), \quad C_{23} = \frac{E_2}{D_0}\left(\nu_{23}\frac{E_3}{E_2}+\nu_{12}\nu_{31}\right), \quad C_{66} = G_{31} \end{aligned} \tag{2.8}$$

with:

$$D_0 = 1-\nu_{12}^2\frac{E_2}{E_1}-\nu_{23}^2\frac{E_3}{E_2}-\nu_{31}^2\frac{E_1}{E_3}-2\nu_{12}\nu_{23}\nu_{31}. \tag{2.9}$$

- **Cubic materials** exhibit not only three orthogonal planes of symmetry but also 90° rotation symmetry with respect to those planes. They are described by three parameters – the Young's modulus E, the Poisson's ratio ν, and the shear modulus G:

$$C_{11} = C_{22} = C_{33} = \frac{E\,(1-\nu)}{(1+\nu)\,(1-2\nu)} \tag{2.10}$$

$$C_{12} = C_{13} = C_{23} = \frac{E\nu}{(1+\nu)\,(1-2\nu)} \tag{2.11}$$

$$C_{33} = C_{55} = C_{66} = G. \tag{2.12}$$

- **Isotropic materials**, such as pure polymers or metals, have an infinite number of symmetry planes. They are defined by two parameters – the Young's modulus E and the Poisson's ratio ν:

$$C_{11} = C_{22} = C_{33} = \frac{E\,(1-\nu)}{(1+\nu)\,(1-2\nu)} \tag{2.13}$$

$$C_{12} = C_{13} = C_{23} = \frac{E\nu}{(1+\nu)\,(1-2\nu)} \tag{2.14}$$

$$C_{44} = C_{55} = C_{66} = \frac{E\left(\frac{1}{2}-\nu\right)}{(1+\nu)\,(1-2\nu)}. \tag{2.15}$$

Substituting Equations (2.4) and (2.6) into Equations (2.1) to (2.3) yields:

$$\int_\Omega (\mathbf{D}\delta\mathbf{u})^T \mathbf{C}(\mathbf{D}\mathbf{u})\, d\Omega = \int_\Omega \delta\mathbf{u}^T \left(\mathbf{b} - \rho\frac{\partial^2\mathbf{u}}{\partial t^2}\right) d\Omega + \int_{\Gamma_t} \delta\mathbf{u}^T\mathbf{t}\, d\Gamma. \tag{2.16}$$

Here, the only unknowns are the displacements $\mathbf{u}$. A numerical approximation of the solution can be obtained by the finite element method. To this end, Ω is divided into finite element domains Ω^e using a mesh. In each domain Ω^e, the displacements $\mathbf{u}^e$ are expressed as a linear combination of known shape functions N_i^e that are defined with respect to the local coordinates ξ, η, and ζ:

$$\mathbf{u}^e \approx \sum_{i=1}^{n} N_i^e(\xi,\eta,\zeta) \begin{bmatrix} d_{\xi,i}^e(t) \\ d_{\eta,i}^e(t) \\ d_{\zeta,i}^e(t) \end{bmatrix} = \mathbf{N}^e\mathbf{d}^e \tag{2.17}$$

where $\mathbf{N}^e$ is the matrix of the local shape functions:

$$\mathbf{N}^e = \begin{bmatrix} N_1^e & 0 & 0 & ... & N_n^e & 0 & 0 \\ 0 & N_1^e & 0 & ... & 0 & N_n^e & 0 \\ 0 & 0 & N_1^e & ... & 0 & 0 & N_n^e \end{bmatrix} \tag{2.18}$$

and $\mathbf{d}^e$ the vector of local degrees of freedom:

$$\mathbf{d}^e = \begin{bmatrix} d_{\xi,1}^e & d_{\eta,1}^e & d_{\zeta,1}^e & ... & d_{\xi,n}^e & d_{\eta,n}^e & d_{\zeta,n}^e \end{bmatrix}^T. \tag{2.19}$$

The local shape functions $\mathbf{N}^e$ vary only in space, whereas the local degrees of freedom $\mathbf{d}^e$ depend only on time. Furthermore, global degrees of freedom $\mathbf{d}$ are introduced and

related to the local ones in order to enforce the continuity of the displacements between elements that share the same topological entities of the mesh such as nodes, edges, or faces. They are associated with global shape functions $\mathbf{N}$, which can be determined from the combination of local ones. The virtual displacements $\delta\mathbf{u}$ are discretized in the same way. Based on this approach, the contributions of the elements are first computed by numerical integration and then assembled, leading to the following semi-discrete system of equations:

$$\mathbf{M}\frac{\partial^2\mathbf{d}}{\partial t^2} + \mathbf{K}\mathbf{d} = \mathbf{f} \tag{2.20}$$

where $\mathbf{M}$ is the mass matrix, and A is the element assembly operator:

$$\begin{aligned}\mathbf{M} &= \int_\Omega \rho\mathbf{N}^T\mathbf{N}\,d\Omega \\ &= \mathop{\mathsf{A}}_{e}\int_{\Omega^e} \rho\mathbf{N}^{eT}\mathbf{N}^e\,d\Omega.\end{aligned} \tag{2.21}$$

$\mathbf{K}$ is the stiffness matrix:

$$\begin{aligned}\mathbf{K} &= \int_\Omega (\mathbf{D}\mathbf{N})^T\mathbf{C}(\mathbf{D}\mathbf{N})\,d\Omega \\ &= \mathop{\mathsf{A}}_{e}\int_{\Omega^e} (\mathbf{D}\mathbf{N}^e)^T\mathbf{C}(\mathbf{D}\mathbf{N}^e)\,d\Omega,\end{aligned} \tag{2.22}$$

and $\mathbf{f}$ is the force vector:

$$\begin{aligned}\mathbf{f} &= \int_\Omega \mathbf{N}^T\mathbf{b}\,d\Omega + \int_{\Gamma_t} \mathbf{N}^T\mathbf{t}\,d\Gamma \\ &= \mathop{\mathsf{A}}_{e}\left(\int_{\Omega^e} \mathbf{N}^{eT}\mathbf{b}\,d\Omega + \int_{\Gamma_t^e} \mathbf{N}^{eT}\mathbf{t}\,d\Gamma\right).\end{aligned} \tag{2.23}$$

Displacement boundary conditions on Γ_d, as shown in Figure 2.1, can be imposed by assigning the values of the known displacements to the respective degrees of freedom and by rearranging the system of equations, which leads to an extended right-hand side. Alternatively, the displacement constraints can be weakly enforced using the Lagrange multiplier or the penalty method [11].

To solve Equation (2.20), a time-integration scheme such as the Newmark method can be applied [18]. This technique is suitable to simulate transient responses and to consider geometric and material nonlinearities. However, high computational costs can arise, for example, if many time steps need to be evaluated. Instead of discretizing the time domain, it can be therefore favorable in the case of periodically excited structures to transfer Equation (2.20) to the frequency domain [21]:

$$\left(-\omega^2\mathbf{M} + \mathbf{K}\right)\hat{\mathbf{d}} = \hat{\mathbf{f}} \tag{2.24}$$

where ω is the angular frequency, and $\hat{\mathbf{d}}$ and $\hat{\mathbf{f}}$ are the Fourier-transform of $\mathbf{d}$ and $\mathbf{f}$:

$$\hat{\mathbf{d}}(\omega) = \int_{-\infty}^{\infty} \mathbf{d}(t)e^{-i\omega t}\,dt \tag{2.25}$$

$$\hat{\mathbf{f}}(\omega) = \int_{-\infty}^{\infty} \mathbf{f}(t)e^{-i\omega t}\,dt. \tag{2.26}$$

Furthermore, solving the eigenproblem:

$$\left(-\omega_i^2\mathbf{M}+\mathbf{K}\right)\mathbf{d}_i=\mathbf{0} \tag{2.27}$$

leads to the natural angular frequencies ω_i and the mode shapes $\mathbf{d}_i$ of the system. They provide important insights when analyzing resonances and are the basis for the mode superposition method, which can enable significant computational savings, especially if only a few modes contribute to the structural response.

2.1.2 Linear viscoelasticity

Viscoelastic material is characterized by strains that develop over time after applying a load. Plus, the strains gradually return to their original state when the load is removed. The material is moreover called linear if its rheological properties do not depend on the strains [22].[b] In the case of periodic excitations, linear viscoelasticity causes a lag between stresses and strains and thus the dissipation of mechanical energy [23].

To represent it, a time-dependent constitutive equation can be employed, for example, derived from the Maxwell, the Kelvin-Voigt, or the Zenner model, which allow for simulating relaxation and creep processes [24]. Furthermore, in the frequency domain, the phase shifts between stresses and strains can be considered by a complex constitutive equation [23]:

$$\hat{\boldsymbol{\sigma}}=\left(\mathbf{C}'+i\mathbf{C}''\right)\hat{\boldsymbol{\varepsilon}} \tag{2.28}$$

where $\mathbf{C}'$ and $\mathbf{C}''$ are the real and the imaginary part of the constitutive matrix. The variables $\hat{\boldsymbol{\sigma}}$ and $\hat{\boldsymbol{\varepsilon}}$ denote the complex amplitudes of the time-harmonic stresses and strains:

$$\boldsymbol{\sigma}(t)=\hat{\boldsymbol{\sigma}}e^{i\omega t}+\hat{\boldsymbol{\sigma}}^*e^{-i\omega t} \tag{2.29}$$

$$\boldsymbol{\varepsilon}(t)=\hat{\boldsymbol{\varepsilon}}e^{i\omega t}+\hat{\boldsymbol{\varepsilon}}^*e^{-i\omega t} \tag{2.30}$$

with $(\cdot)^*$ being the complex conjugate of a variable. In fact, also the time-dependent constitutive equations mentioned above can be expressed in a complex form by introducing time-harmonic stresses and strains, as demonstrated in [24]. Based on this approach, Equation (2.24) turns into a complex system of equations:

$$\left(-\omega^2\mathbf{M}+\hat{\mathbf{K}}\right)\hat{\mathbf{d}}=\hat{\mathbf{f}} \tag{2.31}$$

where $\hat{\mathbf{K}}$ is the complex stiffness matrix of the system:

$$\hat{\mathbf{K}}=\int_\Omega\left(\mathbf{DN}\right)^T\left(\mathbf{C}'+i\mathbf{C}''\right)\left(\mathbf{DN}\right)d\Omega. \tag{2.32}$$

The relation between the constitutive equation, the phase shift, and the energy dissipation is shown in the following for the one-dimensional case. Thus, Equation (2.28) reduces to:

$$\hat{\sigma}=\hat{E}\hat{\varepsilon} \tag{2.33}$$

where $\hat{E}$ is the complex Young's modulus:

$$\hat{E} = E' + iE'' = \left|\hat{E}\right| e^{i\delta} \tag{2.34}$$

with:

$$\left|\hat{E}\right| = \sqrt{E'^2 + E''^2} \tag{2.35}$$

$$\tan\delta = \frac{E''}{E'}. \tag{2.36}$$

The storage modulus E' represents the elastic response, whereas the loss modulus E'' induces a phase shift δ, as illustrated in Figure 2.2 for the subsequent example:

$$\hat{\sigma} = |\hat{\sigma}| \tag{2.37}$$

$$\hat{\varepsilon} = \frac{|\hat{\sigma}|}{\left|\hat{E}\right| e^{i\delta}} = |\hat{\varepsilon}|\, e^{-i\delta}. \tag{2.38}$$

The energy loss W_{loss} per oscillation period, which is equal to the area of the hysteresis loop depicted in Figure 2.3, can be calculated by integrating the strain energy over the duration of a cycle $T = 2\pi/\omega$ [24]:

$$W_{\text{loss}} = \oint \sigma d\varepsilon = \int_0^T \sigma \frac{d\varepsilon}{dt} dt = \pi |\hat{\varepsilon}|^2 E' \tan\delta. \tag{2.39}$$

Therefore, the loss modulus $E'' = E' \tan\delta$ and the loss factor $\eta = \tan\delta$ are important measures for the damping performance of materials.

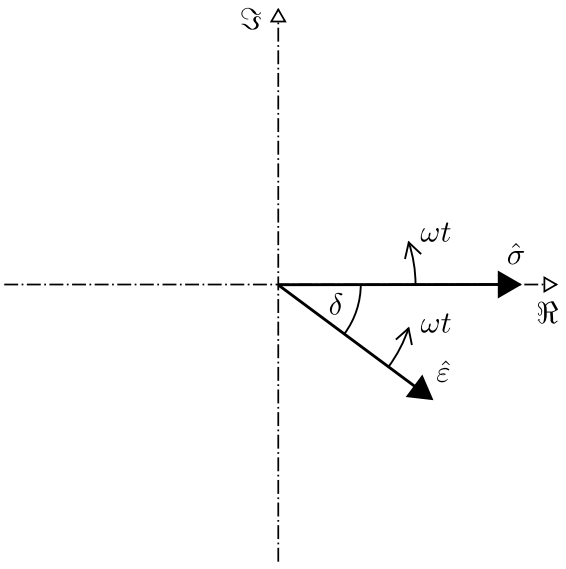

Figure 2.2: Phase shift δ between the stress $\hat{\sigma}$ and the strain $\hat{\varepsilon}$ [25].

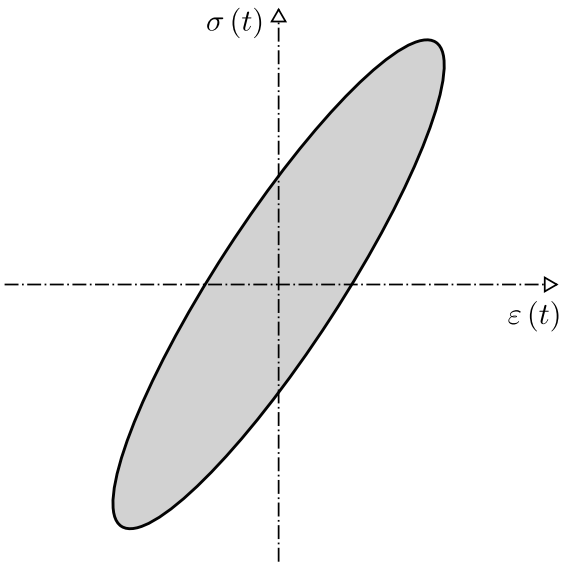

Figure 2.3: Hysteresis loop [24].

Now that the fundamentals of the finite element method have been described for linear elastic and viscoelastic problems, the following sections present techniques to enhance the efficiency of finite element modeling and simulation.

2.2 The p-version of the finite element method

The accuracy of the FE approximation is improved in the p-version by raising the polynomial order p of the element shape functions. This approach can enable significantly faster convergence than the h-version, where the size of low-order elements is reduced. High-order elements moreover exhibit better robustness to mesh distortion and locking effects. Close to singularities, however, the discretization error depends mainly on the element size. Thus, the p-version should be combined with meshes that are gradually refined towards singular points or lines. Furthermore, additional computational savings can be achieved in this efficient discretization strategy by a graded distribution of p, that is, a linear increase from the finest to the coarsest elements [6].

Especially for the p-version of FEM, a hierarchical basis is a well-suited alternative to a standard nodal basis. It is defined by the characteristic that the set of shape functions of order p is included in the set of shape functions of order $p + 1$. The one-dimensional hierarchical basis according to [26] contains integrated Legendre polynomials along with linear shape functions if p is 2 or higher, as depicted in Figure 2.4a. A considerable advantage of this basis is that better conditioning of the stiffness matrix is obtained compared to the standard nodal basis, illustrated in Figure 2.4b [6].[a]

Three-dimensional hierarchical shape functions can be determined from the tensor products of one-dimensional ones and grouped into nodal, edge, face, and internal modes. Nodal modes vanish at every node except for the one they are associated with. The same holds for edge and face modes analogously, whereas internal modes are completely local and vanish at every node, edge, and face. To increase the computational efficiency, the trunk space can be used instead of the tensor product space. It is based on fewer face and internal modes, as shown in [27]. Furthermore, the polynomial orders can be set individually for each local coordinate direction and displacement component. Hexahedral p-elements that exploit these possibilities can represent homogeneous thin-walled structures with approximately the same number of degrees of freedom as dimensionally reduced elements and attain a higher accuracy in addition, as demonstrated in [27].

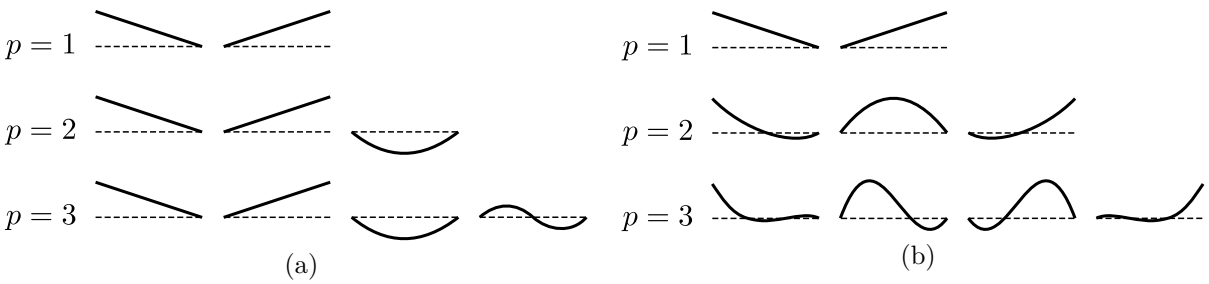

Figure 2.4: Sets of one-dimensional shape functions for $p = 1, 2, 3$: (a) hierarchical basis, (b) standard nodal basis [6].

2.3 The finite cell method

The creation of three-dimensional FE meshes for complex structures starting from CAD models or digital images is generally a non-trivial task that can require significant manual work. This is especially the case for the p-version of FEM, where the domain of computation needs to be represented by only a small number of elements. Apart from intricate geometric features, flaws in CAD models such as gaps and overlaps can complicate mesh generation [8]. As a fictitious domain approach, the finite cell method can bypass these problems because it only relies on simple non-boundary-conforming meshes and point-inclusion tests that can be performed directly on the original geometric representations, such as Brep models [8], CSG models [28], CT scans [29], and point clouds [30]. The FCM thus offers a substantially simplified modeling procedure. Moreover, it allows for fast convergence rates by employing high-order shape functions [6].

In the FCM, the physical domain Ω is embedded in an extended domain Ω_{ext}, as depicted for two dimensions in Figure 2.5. Hence, the original elastic problem given in Equation (2.16) is replaced by the following auxiliary problem:

$$\int_{\Omega_{\text{ext}}} (\mathbf{D}\delta\mathbf{u})^T \alpha \mathbf{C}(\mathbf{D}\mathbf{u})\, d\Omega = \int_{\Omega_{\text{ext}}} \delta\mathbf{u}^T \left(\alpha\mathbf{b} - \alpha\rho\frac{\partial^2\mathbf{u}}{\partial t^2}\right) d\Omega + \int_{\Gamma_t} \delta\mathbf{u}^T\mathbf{t}\, d\Gamma \tag{2.40}$$

where the indicator function α depends on the position $\mathbf{x}$. It is 1 inside of Ω and close to 0 outside of it:

$$\alpha(\mathbf{x}) = 1.0 \quad \forall\, \mathbf{x} \in \Omega \tag{2.41}$$

$$0.0 < \alpha(\mathbf{x}) \ll 1.0 \quad \forall\, \mathbf{x} \notin \Omega. \tag{2.42}$$

Therefore, the stiffness, density, and body force almost vanish in the fictitious domain $\Omega_{\text{fict}} = \Omega_{\text{ext}} \backslash \Omega$. The non-zero value of the indicator function α outside of Ω serves to improve the conditioning of the system of equations resulting from the discretization of Ω_{ext}. It is usually set between 10^{-6} and 10^{-12} such that the modeling error added to the original problem is marginal [6].

The extended domain Ω_{ext} can be easily meshed without considering the boundary of the physical domain $\partial\Omega$. This is because α resolves the geometry of Ω when the matrices of the finite elements, also called finite cells, are integrated. However, finite cells cut by the boundary $\partial\Omega$ have a discontinuous integrand. As the Gauss quadrature converges only slowly in this case, special integration schemes, for example based on spacetrees [28–30], smart octrees [31, 32], or moment-fitting [32, 33], are employed to

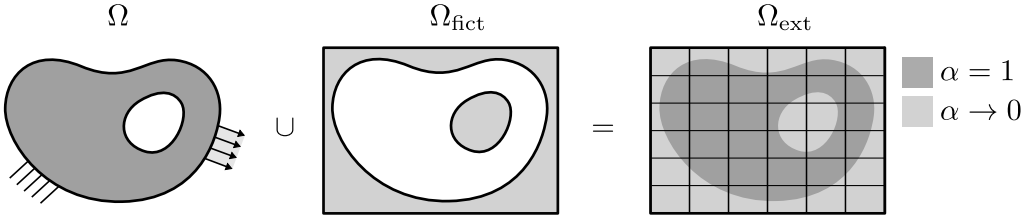

Figure 2.5: The physical domain Ω is embedded in the extended domain Ω_{ext} and resolved by the indicator function α during the integration of the element matrices [6].[e]

reduce the integration error to a negligible level [34]. Particular treatment is also necessary for boundary conditions that are not aligned to the finite cell mesh. For instance, traction and weak displacement boundary conditions can be imposed using suitable surface meshes for numerical integration [6].

2.4 The mortar finite element method [b]

The mortar method allows the components of a structure to be discretized independently. In this way, numerical models can be created more easily. Also, both p-FEM and FCM can be employed in the same model. The classical mortar approach imposes a rigid connection between the components. It is first described in this section before the modified mortar method is presented, which can additionally represent a thin damping layer between the components in a dimensionally reduced way.

2.4.1 Mesh coupling

If the components of a structure are meshed independently, the numerical model does not consist of a single domain Ω but of several subdomains Ω_i. Further, the continuity of the displacements between the subdomains Ω_i is not imposed by shared element nodes, edges, or faces. However, it can be enforced in a weak form by applying the mortar method. For simplicity of notation, the case of two subdomains Ω_1 and Ω_2 with an interface Γ_I is considered in the following, as illustrated in Figure 2.6. The two adjacent subdomains of Γ_I are referred to as the *mortar (M)* and the *non-mortar (S)* side. Hence, $\mathbf{u}_M$ and $\mathbf{u}_S$ denote the deformations $\mathbf{u}_1$ and $\mathbf{u}_2$ at Γ_I:

$$\begin{aligned} \mathbf{u}_M &= \mathbf{u}_1|_{\Gamma_I} \\ \mathbf{u}_S &= \mathbf{u}_2|_{\Gamma_I}. \end{aligned}$$

In the mortar method, the virtual work δW_I of the tractions $\mathbf{t}_M$ and $\mathbf{t}_S$ on Γ_I is taken into account as external work:

$$\delta W_I = \int_{\Gamma_I} \left(\delta \mathbf{u}_S^T \mathbf{t}_S + \delta \mathbf{u}_M^T \mathbf{t}_M \right) d\Gamma. \tag{2.43}$$

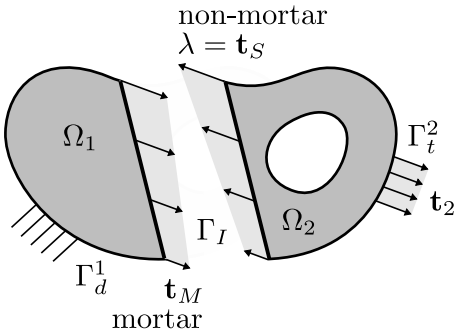

Figure 2.6: Two domains Ω_1 and Ω_2 coupled by the mortar method.

Since $\mathbf{t}_M$ and $\mathbf{t}_S$ are unknown, Lagrange multipliers $\boldsymbol{\lambda}$ that are equal to $\mathbf{t}_S$ and in balance with $\mathbf{t}_M$ are introduced [11, 17]:

$$\boldsymbol{\lambda} = \mathbf{t}_S = -\mathbf{t}_M. \tag{2.44}$$

The total virtual work is therefore:

$$\begin{aligned}
&\int_{\Omega_1} \left[(\mathbf{D}\delta\mathbf{u}_1)^T \mathbf{C}_1 (\mathbf{D}\mathbf{u}_1) - \delta\mathbf{u}_1^T \left(\mathbf{b}_1 - \rho \frac{\partial^2 \mathbf{u}_1}{\partial t^2} \right) \right] d\Omega - \int_{\Gamma_t^1} \delta\mathbf{u}_1^T \mathbf{t}_1 d\Gamma \\
&+ \int_{\Omega_2} \left[(\mathbf{D}\delta\mathbf{u}_2)^T \mathbf{C}_2 (\mathbf{D}\mathbf{u}_1) - \delta\mathbf{u}_2^T \left(\mathbf{b}_2 - \rho \frac{\partial^2 \mathbf{u}_2}{\partial t^2} \right) \right] d\Omega - \int_{\Gamma_t^2} \delta\mathbf{u}_2^T \mathbf{t}_2 d\Gamma \\
&- \int_{\Gamma_I} \left[(\delta\mathbf{u}_S - \delta\mathbf{u}_M)^T \boldsymbol{\lambda} \right] d\Gamma = 0.
\end{aligned} \tag{2.45}$$

Moreover, to weakly impose the continuity of the displacements across Γ_I, Equation (2.45) is supplemented by the constraint equation:

$$\int_{\Gamma_I} \delta\boldsymbol{\lambda}^T (\mathbf{u}_M - \mathbf{u}_S)\, d\Gamma = 0. \tag{2.46}$$

Inserting the approximations:

$$\begin{aligned}
\mathbf{u}_1 &\approx \mathbf{N}_1 \mathbf{d}_1 & \delta\mathbf{u}_1 &\approx \mathbf{N}_1 \delta\mathbf{d}_1 \\
\mathbf{u}_2 &\approx \mathbf{N}_2 \mathbf{d}_2 & \delta\mathbf{u}_2 &\approx \mathbf{N}_2 \delta\mathbf{d}_2 \\
\boldsymbol{\lambda} &\approx \mathbf{N}_\lambda \mathbf{d}_\lambda & \delta\boldsymbol{\lambda} &\approx \mathbf{N}_\lambda \delta\mathbf{d}_\lambda
\end{aligned} \tag{2.47}$$

into Equations (2.45) and (2.46) leads to the following system of equations [11]:

$$\begin{bmatrix} \mathbf{M}_1 & \mathbf{0} & \mathbf{0} \\ \mathbf{0} & \mathbf{M}_2 & \mathbf{0} \\ \mathbf{0} & \mathbf{0} & \mathbf{0} \end{bmatrix} \frac{\partial^2}{\partial t^2} \begin{pmatrix} \mathbf{d}_1 \\ \mathbf{d}_2 \\ \mathbf{d}_\lambda \end{pmatrix} + \begin{bmatrix} \mathbf{K}_1 & \mathbf{0} & \mathbf{G}_1 \\ \mathbf{0} & \mathbf{K}_2 & \mathbf{G}_2 \\ \mathbf{G}_1^T & \mathbf{G}_2^T & \mathbf{0} \end{bmatrix} \begin{pmatrix} \mathbf{d}_1 \\ \mathbf{d}_2 \\ \mathbf{d}_\lambda \end{pmatrix} = \begin{pmatrix} \mathbf{f}_1 \\ \mathbf{f}_2 \\ \mathbf{0} \end{pmatrix} \tag{2.48}$$

where:

$$\begin{aligned}
\mathbf{M}_1 &= \int_{\Omega_1} \rho_1 \mathbf{N}_1^T \mathbf{N}_1\, d\Omega & \mathbf{M}_2 &= \int_{\Omega_2} \rho_2 \mathbf{N}_2^T \mathbf{N}_2\, d\Omega \\
\mathbf{K}_1 &= \int_{\Omega_1} (\mathbf{D}\mathbf{N}_1)^T \mathbf{C}_1 (\mathbf{D}\mathbf{N}_1)\, d\Omega & \mathbf{K}_2 &= \int_{\Omega_2} (\mathbf{D}\mathbf{N}_2)^T \mathbf{C}_2 (\mathbf{D}\mathbf{N}_2)\, d\Omega \\
\mathbf{G}_1 &= \int_{\Gamma_I} \mathbf{N}_1^T \mathbf{N}_\lambda\, d\Gamma & \mathbf{G}_2 &= -\int_{\Gamma_I} \mathbf{N}_2^T \mathbf{N}_\lambda\, d\Gamma \\
\mathbf{f}_1 &= \int_{\Omega_1} \mathbf{N}_1^T \mathbf{b}\, d\Omega + \int_{\Gamma_t^1} \mathbf{N}_1^T \mathbf{t}\, d\Gamma & \mathbf{f}_2 &= \int_{\Omega_2} \mathbf{N}_2^T \mathbf{b}\, d\Omega + \int_{\Gamma_t^2} \mathbf{N}_2^T \mathbf{t}\, d\Gamma.
\end{aligned} \tag{2.49}$$

According to Equation (2.48), the domains Ω_1 and Ω_2 are coupled by the submatrices $\mathbf{G}_1$ and $\mathbf{G}_2$ determined from the integrals over Γ_I. The shape functions $\mathbf{N}_\lambda$ are equal to those defined on the non-mortar boundary, which belongs in the considered case to the domain Ω_2 [35]:

$$N_{\lambda,i} = N_{2,i}|_{\Gamma_I}. \tag{2.50}$$

The vibration behavior of the complete structure, including material damping, can be computed by transferring Equation (2.48) to the frequency domain and by introducing complex constitutive relations:

$$\left(-\omega^2 \begin{bmatrix} \mathbf{M}_1 & \mathbf{0} & \mathbf{0} \\ \mathbf{0} & \mathbf{M}_2 & \mathbf{0} \\ \mathbf{0} & \mathbf{0} & \mathbf{0} \end{bmatrix} + \begin{bmatrix} \hat{\mathbf{K}}_1 & \mathbf{0} & \mathbf{G}_1 \\ \mathbf{0} & \hat{\mathbf{K}}_2 & \mathbf{G}_2 \\ \mathbf{G}_1^T & \mathbf{G}_2^T & \mathbf{0} \end{bmatrix}\right) \begin{pmatrix} \hat{\mathbf{d}}_1 \\ \hat{\mathbf{d}}_2 \\ \hat{\mathbf{d}}_\lambda \end{pmatrix} = \begin{pmatrix} \hat{\mathbf{f}}_1 \\ \hat{\mathbf{f}}_2 \\ \mathbf{0} \end{pmatrix} \tag{2.51}$$

with:

$$\hat{\mathbf{K}}_1 = \int_{\Omega_1} (\mathbf{D}\mathbf{N}_1)^T \left(\mathbf{C}_1' + i\mathbf{C}_1''\right) (\mathbf{D}\mathbf{N}_1)\, d\Omega \tag{2.52}$$

$$\hat{\mathbf{K}}_2 = \int_{\Omega_2} (\mathbf{D}\mathbf{N}_2)^T \left(\mathbf{C}_2' + i\mathbf{C}_2''\right) (\mathbf{D}\mathbf{N}_2)\, d\Omega. \tag{2.53}$$

Furthermore, the natural frequencies ω_i and the mode shapes $[\mathbf{d}_{1,i}\ \mathbf{d}_{2,i}]^T$ can be determined by solving:

$$\left(-\omega_i^2 \begin{bmatrix} \mathbf{M}_1 & \mathbf{0} & \mathbf{0} \\ \mathbf{0} & \mathbf{M}_2 & \mathbf{0} \\ \mathbf{0} & \mathbf{0} & \mathbf{0} \end{bmatrix} + \begin{bmatrix} \mathbf{K}_1 & \mathbf{0} & \mathbf{G}_1 \\ \mathbf{0} & \mathbf{K}_2 & \mathbf{G}_2 \\ \mathbf{G}_1^T & \mathbf{G}_2^T & \mathbf{0} \end{bmatrix}\right) \begin{pmatrix} \mathbf{d}_{1,i} \\ \mathbf{d}_{2,i} \\ \mathbf{d}_{\lambda,i} \end{pmatrix} = \mathbf{0}. \tag{2.54}$$

However, damping effects are not considered here.

2.4.2 Mortar formulation including viscoelastic layers

The mortar method presented above was modified in [17] to model isotropic linear elastic layers between separately discretized components in a dimensionally reduced way, as illustrated in Figure 2.7. The mass of the layer is neglected therein, and damping effects are not considered. Papers B and E further extended this approach to orthotropic linear viscoelastic layers such that frequency response analyses can be performed accurately for various materials, such as elastomers and high damping composites.

In the modified mortar formulation, the continuity constraint described in Equation (2.46) is replaced by a coupling condition that represents a solid layer with the constant thickness b_L between Ω_1 and Ω_2. To this end, first, a two-dimensional local coordinate system (x^*, y^*) is introduced along the interface Γ_I and extended by a third basis vector which is perpendicular to Γ_I, as depicted in Figure 2.8. Its corresponding coordinate z^* is zero on the non-mortar side and b_L on the mortar side. Secondly, it is assumed that the sum of the virtual work of $\boldsymbol{\lambda}$ on the non-mortar side is equal to that of the tractions $\mathbf{t}_L$ on the cut plane through the layer at $z^* = 0$ [17]:

$$\int_{\Gamma_I} \delta\mathbf{u}_S^T(\mathbf{t}_L - \boldsymbol{\lambda}) d\Gamma = 0 \tag{2.55}$$

where:

$$\mathbf{t}_L = \begin{bmatrix} \sigma_{L,x^*z^*}(z^* = 0) \\ \sigma_{L,y^*z^*}(z^* = 0) \\ \sigma_{L,z^*z^*}(z^* = 0) \end{bmatrix}. \tag{2.56}$$

The variable $\boldsymbol{\sigma}_L$ denotes the stress state in the complete layer with respect to the local coordinate system. Based on the linear ansatz for the displacements $\mathbf{u}_L$ of the layer according to [17]:

$$\mathbf{u}_L = \mathbf{u}_S + \frac{z^*}{b_L}(\mathbf{u}_M - \mathbf{u}_S), \tag{2.57}$$

the stresses $\boldsymbol{\sigma}_L$ can be stated as a function of $\mathbf{u}_S$ and $\mathbf{u}_M$ by applying the constitutive relations:

$$\boldsymbol{\sigma}_L = \mathbf{C}_L \boldsymbol{\varepsilon}_L \tag{2.58}$$

and the kinematic relations:

$$\boldsymbol{\varepsilon}_L = \mathbf{D}_L \mathbf{u}_L \tag{2.59}$$

where $\mathbf{D}_L$ is the local partial differential operator:

$$\mathbf{D}_L^T = \begin{bmatrix} \frac{\partial}{\partial x^*} & 0 & 0 & \frac{\partial}{\partial y^*} & 0 & \frac{\partial}{\partial z^*} \\ 0 & \frac{\partial}{\partial y^*} & 0 & \frac{\partial}{\partial x^*} & \frac{\partial}{\partial z^*} & 0 \\ 0 & 0 & \frac{\partial}{\partial z^*} & 0 & \frac{\partial}{\partial y^*} & \frac{\partial}{\partial x^*} \end{bmatrix}. \tag{2.60}$$

Combining Equations (2.55) to (2.59) leads to:

$$\begin{aligned} \int_{\Gamma_I} \delta\mathbf{u}_S^T \Bigg[& \begin{pmatrix} C_{L,61} \\ C_{L,51} \\ C_{L,31} \end{pmatrix} \frac{\partial u_{Sx^*}}{\partial x^*} + \begin{pmatrix} C_{L,62} \\ C_{L,52} \\ C_{L,32} \end{pmatrix} \frac{\partial u_{Sy^*}}{\partial y^*} + \begin{pmatrix} C_{L,63} \\ C_{L,53} \\ C_{L,33} \end{pmatrix} \frac{u_{Mz^*} - u_{Sz^*}}{b_L} + \begin{pmatrix} C_{L,64} \\ C_{L,54} \\ C_{L,34} \end{pmatrix} \left(\frac{\partial u_{Sx^*}}{\partial y^*} + \frac{\partial u_{Sy^*}}{\partial x^*} \right) \\ & + \begin{pmatrix} C_{L,65} \\ C_{L,55} \\ C_{L,35} \end{pmatrix} \left(\frac{\partial u_{Sz^*}}{\partial y^*} + \frac{u_{My^*} - u_{Sy^*}}{b_L} \right) + \begin{pmatrix} C_{L,66} \\ C_{L,56} \\ C_{L,36} \end{pmatrix} \left(\frac{\partial u_{Sz^*}}{\partial x^*} + \frac{u_{Mx^*} - u_{Sx^*}}{b_L} \right) \Bigg] - \delta\mathbf{u}_S^T \boldsymbol{\lambda} \, d\Gamma = \mathbf{0}. \end{aligned} \tag{2.61}$$

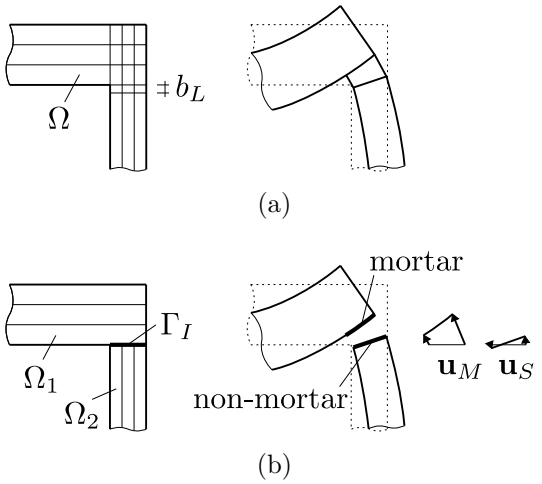

Figure 2.7: FE models of a structure including an elastic/viscoelastic layer based on: (a) one conforming mesh, (b) two non-matching meshes coupled by the modified mortar method.[b]

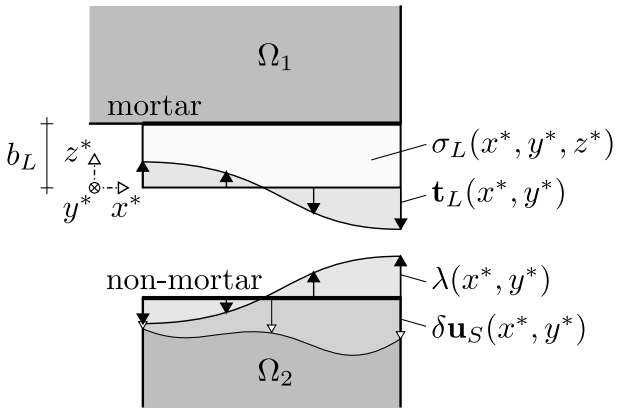

Figure 2.8: Stresses at the interface Γ_I.[b]

In the case of an orthotropic stiffness matrix $\mathbf{C}_L$, Equation (2.61) can be simplified to:

$$\int_{\Gamma_I} \delta\mathbf{u}_S^T \begin{pmatrix} C_{L,66}\left(\frac{\partial u_{Sz^*}}{\partial x^*} + \frac{u_{Mx^*}-u_{Sx^*}}{b_L}\right) \\ C_{L,55}\left(\frac{\partial u_{Sz^*}}{\partial y^*} + \frac{u_{My^*}-u_{Sy^*}}{b_L}\right) \\ C_{L,31}\frac{\partial u_{Sx^*}}{\partial x^*} + C_{L,32}\frac{\partial u_{Sy^*}}{\partial y^*} + C_{L,33}\frac{u_{Mz^*}-u_{Sz^*}}{b_L} \end{pmatrix} - \delta\mathbf{u}_S^T\boldsymbol{\lambda}\, d\Gamma = \mathbf{0}. \tag{2.62}$$

After the discretization, the following unsymmetric system of equations is obtained from Equations (2.45) and (2.62):

$$\begin{bmatrix} \mathbf{M}_1 & \mathbf{0} & \mathbf{0} \\ \mathbf{0} & \mathbf{M}_2 & \mathbf{0} \\ \mathbf{0} & \mathbf{0} & \mathbf{0} \end{bmatrix} \frac{\partial^2}{\partial t^2} \begin{pmatrix} \mathbf{d}_1 \\ \mathbf{d}_2 \\ \mathbf{d}_\lambda \end{pmatrix} + \begin{bmatrix} \mathbf{K}_1 & \mathbf{0} & \mathbf{G}_1 \\ \mathbf{0} & \mathbf{K}_2 & \mathbf{G}_2 \\ \mathbf{P}_1 & \mathbf{P}_2 & \mathbf{Q} \end{bmatrix} \begin{pmatrix} \mathbf{d}_1 \\ \mathbf{d}_2 \\ \mathbf{d}_\lambda \end{pmatrix} = \begin{pmatrix} \mathbf{f}_1 \\ \mathbf{f}_2 \\ \mathbf{0} \end{pmatrix} \tag{2.63}$$

where the submatrices $\mathbf{P}_1$, $\mathbf{P}_2$, and $\mathbf{Q}$ are derived from the modified coupling condition (2.62):

$$\mathbf{P}_1 = \int_{\Gamma_I} \mathbf{N}_2^T \begin{bmatrix} \frac{C_{L,66}}{b_L} & 0 & 0 \\ 0 & \frac{C_{L,55}}{b_L} & 0 \\ 0 & 0 & \frac{C_{L,33}}{b_L} \end{bmatrix} \mathbf{N}_1\, d\Gamma \tag{2.64}$$

$$\mathbf{P}_2 = \int_{\Gamma_I} -\mathbf{N}_2^T \begin{bmatrix} \frac{C_{L,66}}{b_L} & 0 & 0 \\ 0 & \frac{C_{L,55}}{b_L} & 0 \\ 0 & 0 & \frac{C_{L,33}}{b_L} \end{bmatrix} \mathbf{N}_2 + \mathbf{N}_2^T \begin{pmatrix} C_{66}\frac{\partial \mathbf{N}_2^{z^*}}{\partial x^*} \\ C_{55}\frac{\partial \mathbf{N}_2^{z^*}}{\partial y^*} \\ C_{31}\frac{\partial \mathbf{N}_2^{x^*}}{\partial x^*} + C_{32}\frac{\partial \mathbf{N}_2^{y^*}}{\partial y^*} \end{pmatrix} d\Gamma \tag{2.65}$$

$$\mathbf{Q} = -\int_{\Gamma_I} \mathbf{N}_2^T \mathbf{N}_\lambda\, d\Gamma. \tag{2.66}$$

The vectors $\mathbf{N}_2^{x^*}$, $\mathbf{N}_2^{y^*}$, and $\mathbf{N}_2^{z^*}$ denote the global shape functions of Ω_2 with respect to the local coordinate system of the layer. For example, if the basis vectors of the global coordinate system are equal to those of the local one, it holds that:

$$\mathbf{N}_2 = \begin{pmatrix} \mathbf{N}_2^{x^*} \\ \mathbf{N}_2^{y^*} \\ \mathbf{N}_2^{z^*} \end{pmatrix}. \tag{2.67}$$

Transferring Equation (2.63) to the frequency domain and using complex constitutive relations:

$$\hat{\boldsymbol{\sigma}}_L = \left(\mathbf{C}_L' + i\mathbf{C}_L''\right)\hat{\boldsymbol{\varepsilon}}_L \tag{2.68}$$

enables vibration analyses that consider the effect of a linear viscoelastic layer between the domains Ω_1 and Ω_2:

$$\left(-\omega^2 \begin{bmatrix} \mathbf{M}_1 & \mathbf{0} & \mathbf{0} \\ \mathbf{0} & \mathbf{M}_2 & \mathbf{0} \\ \mathbf{0} & \mathbf{0} & \mathbf{0} \end{bmatrix} + \begin{bmatrix} \hat{\mathbf{K}}_1 & \mathbf{0} & \mathbf{G}_1 \\ \mathbf{0} & \hat{\mathbf{K}}_2 & \mathbf{G}_2 \\ \hat{\mathbf{P}}_1 & \hat{\mathbf{P}}_2 & \mathbf{Q} \end{bmatrix}\right) \begin{pmatrix} \hat{\mathbf{d}}_1 \\ \hat{\mathbf{d}}_2 \\ \hat{\mathbf{d}}_\lambda \end{pmatrix} = \begin{pmatrix} \hat{\mathbf{f}}_1 \\ \hat{\mathbf{f}}_2 \\ \mathbf{0} \end{pmatrix}. \tag{2.69}$$

Here, the damping properties of the layer are included in the imaginary parts of the complex submatrices $\hat{\mathbf{P}}_1$ and $\hat{\mathbf{P}}_2$. The equation for modal analysis is moreover given by:

$$\left(-\omega_i^2 \begin{bmatrix} \mathbf{M}_1 & \mathbf{0} & \mathbf{0} \\ \mathbf{0} & \mathbf{M}_2 & \mathbf{0} \\ \mathbf{0} & \mathbf{0} & \mathbf{0} \end{bmatrix} + \begin{bmatrix} \mathbf{K}_1 & \mathbf{0} & \mathbf{G}_1 \\ \mathbf{0} & \mathbf{K}_2 & \mathbf{G}_2 \\ \mathbf{P}_1 & \mathbf{P}_2 & \mathbf{Q} \end{bmatrix} \right) \begin{pmatrix} \mathbf{d}_{1,i} \\ \mathbf{d}_{2,i} \\ \mathbf{d}_{\lambda,i} \end{pmatrix} = \mathbf{0}. \tag{2.70}$$

The following chapters summarize Papers A to E and discuss the results. In this context, the accuracy and efficiency of the presented numerical methods are verified by various examples.

Chapter 3

Analysis of cross-laminated timber assemblies

Production of CLT has grown rapidly since it started about twenty years ago [36]. This development can be attributed to the increasing popularity of wood as sustainable raw material and to the particular benefits of CLT products arising from their structure. They comprise layers of wooden boards, which are glued together crosswise to each other. Thus, in- and out-of-plane loads are transferred such that load-carrying walls and ceilings can be made of connected CLT elements without additional structural components. Furthermore, CLT constructions are characterized by less air permeability and higher heat storage capacity than timber frame structures. Compared to reinforced concrete, a higher degree of prefabrication and less structural weight can be achieved with CLT [2]. Alongside many advantages, however, noise insulation should be considered carefully when planning a building made of solid wood. In order to predict the vibration behavior of CLT assemblies, the characteristics of the components such as orthotropy of the raw material, differently directed layers, high shear deformations of transversely oriented layers, and biaxial load transfer need to be taken into account [37]. Furthermore, the connections, which can contain elastomers to reduce flanking transmission, must be modeled properly because complex three-dimensional strain states can occur there.[a]

In Papers A, B, and C, high-order hexahedral finite element models for CLT assemblies are presented. They allow for accurate and efficient vibration computations in the low frequency range even if elastomer layers are placed in between the components. In these models, the layers are represented either by conforming finite elements or by the modified mortar coupling. The validation was carried out in two steps. First, the accuracy of conforming FE models was evaluated in Paper A based on measurements. Secondly, non-conforming FE models employing the modified mortar method were verified in Paper B by comparing their results to those of the conforming ones. Moreover, the good suitability of the mortar-based approach to analyze complete multistory buildings was demonstrated in Paper C.

3.1 Validation of conforming high-order FE models [a]

Paper A provides a modeling approach for CLT assemblies based on conforming high-order FE elements. To validate it, experimental tests were performed in the laboratory for sound measurements at Rosenheim University of Applied Sciences [38]. In the following, the test structures and measurements are briefly described. Then, the modeling technique is demonstrated on the given example before the results are finally discussed.

3.1.1 Test structures and measurements

The test structure depicted in Figure 3.1 consists of two building components, a ceiling and a wall. Each of them is made of CLT panels linked by wooden top boards [39, 40]. The components are screwed together and have hinged supports, the wall at the bottom and the ceiling at the edge opposite to the bolted connection. Moreover, two variants are considered: In one case, there is a 12.5 mm thick elastomer layer between the components (Figure 3.1b), and in the other case, the ceiling is placed directly on top of the wall (Figure 3.1c).

A sine-sweep excitation was induced by an electrodynamic shaker successively at two points. One was placed at the ceiling and the other at the wall, as shown in Figure 3.1a. Furthermore, accelerometers were arranged in irregular grids across the surfaces of the components and an impedance head was deployed at the respective excitation point to determine the complex transfer accelerances for each load case. Based on the measured frequency response functions, the natural frequencies and mode shapes were determined by the peak amplitude method [41]. Therein, the peak values of the imaginary part of the transfer accelerances serve as an approximation of the mode shapes. Although the accuracy can be decreased by the influence of off-resonant modes, this technique is well suited here since many well-separated modes occur in the considered frequency range from 20 Hz to 150 Hz.

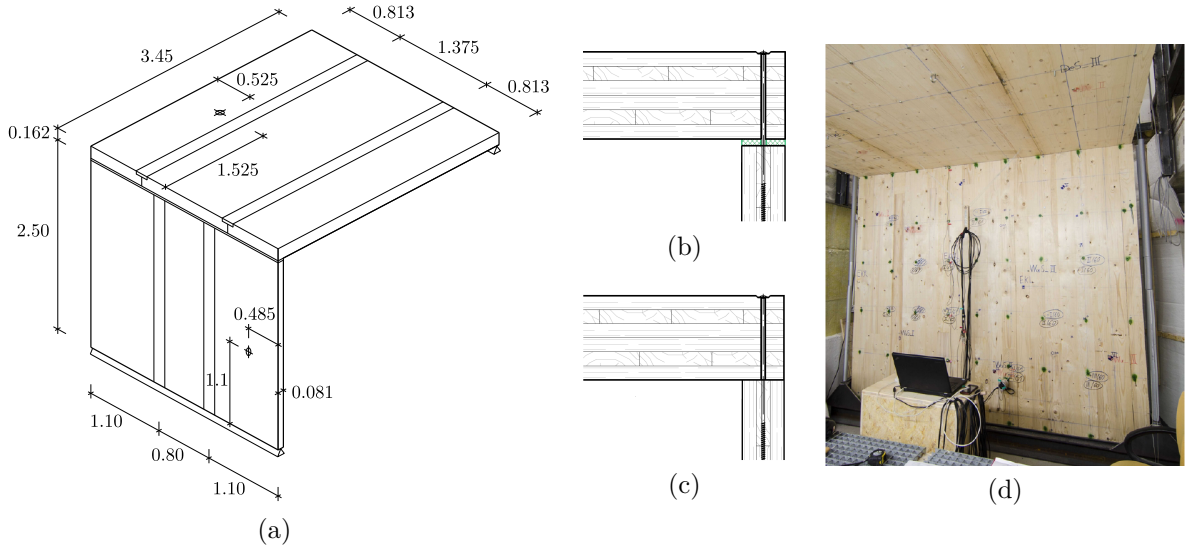

Figure 3.1: Test structure: (a) dimensions and excitation points [m], (b) connection with elastomer, (c) connection without elastomer, (d) measurement setup [38].[a]

After the measurements on the assembly, the wall was detached from the ceiling, hung up such that it could deform freely, and tested in the same way to identify its natural frequencies and mode shapes without the influence of the connection to the ceiling.

3.1.2 Finite element models

The test structures are represented by hexahedral finite elements with hierarchical shape functions. The polynomial degrees p range from 2 to 4 such that the elements can have large aspect ratios, as depicted in Figure 3.2. Therefore, the FE model of the assembly comprises only 747 elements and that of the wall only 90 elements even though they resolve each layer of the CLT panels individually. Furthermore, the hinged support conditions of the assembly are enforced by fixing element edges, as shown in Figure 3.2b.

Different linear viscoelastic materials are assigned to the finite elements, depending on which structural part is modeled:

(a) the CLT layers,
(b) the connections of the CLT panels by the wooden top boards,
(c) the connection of the wall to the ceiling.

Orthotropic constitutive relations are employed for (a) and (b). The values of the material parameters for (a) are taken from technical standards [42, 43] and measurements [44, 38]. In addition, missing narrow face bonding is considered by reducing the in-plane Young's modulus perpendicular to the board direction E_2^{CLT} and the in-plane shear modulus G_{12}^{CLT}. To this end, they are multiplied by the factors κ_1 and κ_2, respectively. The parameters for (b) are calculated from a beam analogy that adapts the material properties of the top boards, given in [40], to the corresponding FE representation. To model (c), whether with or without elastomer, isotropic material with the Young's modulus E_L and the Poisson's ratio ν_L is assigned to a 12.5 mm thick layer of finite elements between the components.

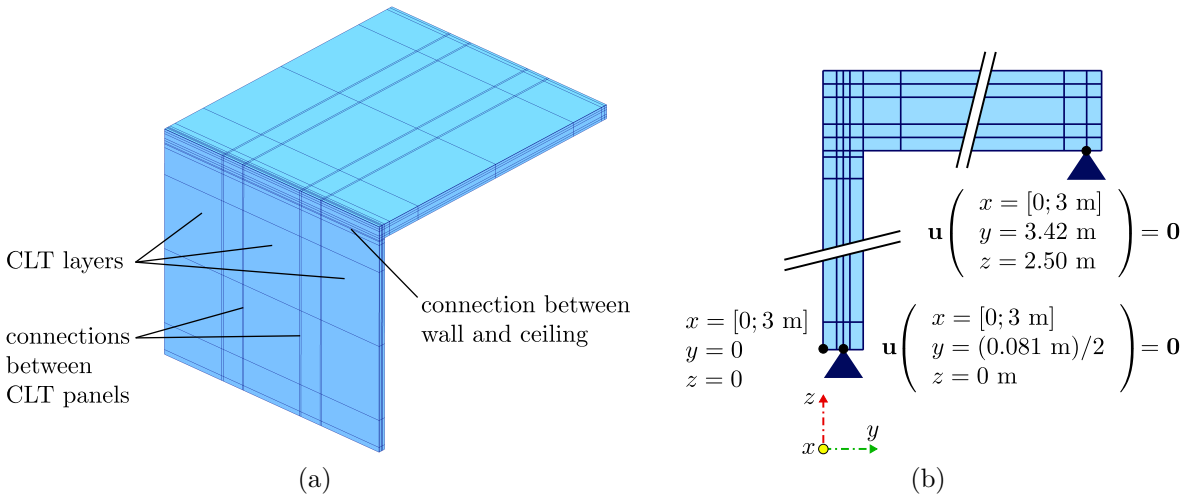

Figure 3.2: Conforming FE mesh of the test structure: (a) total view, (b) details and boundary conditions.[a]

3.1.3 Modal analysis

The FE models were validated and suitable values for κ_1 and κ_2 as well as for E_L and ν_L were determined by comparing simulations with measurements. For this purpose, the natural frequencies of the test structures were computed under variation of the aforementioned parameters, and their root mean square error ε_f with respect to the measurement results was calculated in each case. The correct assignment of the modes was enabled by the modal assurance criterion (MAC) [45].

If $\kappa_1 = \kappa_2 = 1$, meaning that E_2^{CLT} and G_{12}^{CLT} are not reduced, a rather high ε_f of 8.73 % occurs in the case of the free-hanging wall. Therefore, missing narrow face bonding should be taken into account. Best correspondence between computation and measurement is achieved with $\kappa_1 = 0.85$ and $\kappa_2 = 0.70$. Here, the error ε_f is only 2.5 %. In the subsequent FE calculations of the assembled test structure, κ_1 and κ_2 are fixed at the optimal values, while E_L and ν_L are varied:

- Without elastomer, there is only a little dependency of ε_f on the Poisson's ratio ν_L. The flattest minimum of ε_f is reached at $\nu_L = 0$. In this case, ε_f is less than 5 % if E_L is in the range between 5.0 N/mm^2 and 148.0 N/mm^2. With 2.9 %, the lowest ε_f occurs at $E_L = 19$ N/mm^2. Thus, the material assigned to the elements representing the screwed connection without elastomer needs to be significantly less stiff than timber.
- To model the junction with elastomer, the Young's modulus E_L must be chosen even lower, and the dependency of the results on the Poisson's ratio ν_L is higher. The smallest ε_f is 1.7 %. It occurs at $E_L = 2.1$ N/mm^2 and $\nu_L = 0.48$. Apart from

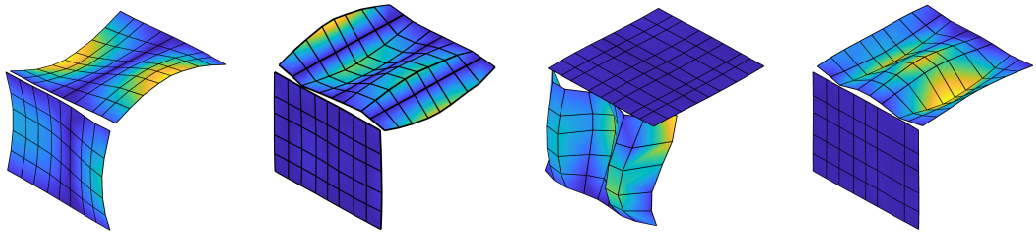

(a) (b) (c) (d)

Figure 3.3: Examples of measured natural frequencies and related mode shapes of the test structure with elastomer: (a) 29.0 Hz, (b) 54.0 Hz, (c) 74.8 Hz, (d) 130.0 Hz.[a]

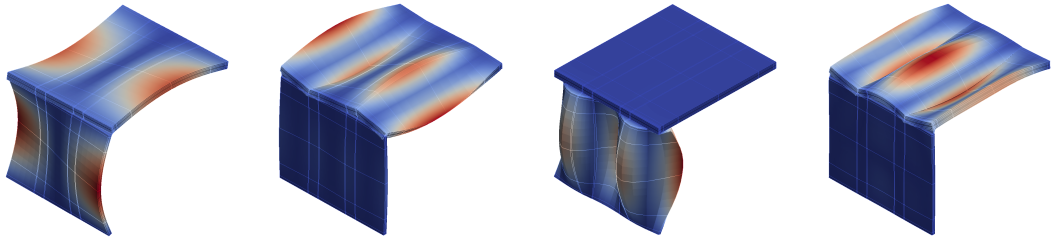

(a) (b) (c) (d)

Figure 3.4: Examples of calculated natural frequencies and related mode shapes of the test structure with elastomer: (a) 28.6 Hz, (b) 50.6 Hz, (c) 73.9 Hz, (d) 130.0 Hz.[a]

this, the isotropic material parameters of the elastomer can be derived from the manufacturer's data sheet [46] using the method presented by Negreira et al. [22]. A unique solution for the Young's modulus and the Poisson's ratio was found since the static shear modulus of the elastomer is known from experimental tests according to [47]. Employing these values to represent the screw connection with elastomer, that is, $E_L = 2.28$ N/mm^2 and $\nu_L = 0.386$ leads to a low error ε_f of 2.8 %. Without additional measurements, multiple solutions are obtained by the approach given in [22]. In this case, ε_f is less than 5 % if the Poisson's ratio is selected in the range between 0.29 and 0.44. This shows that the material parameters of the elastomer are well suited for the representation of this connection.

The effect of hierarchical high-order shape functions on the computational efficiency is investigated using the example of the assembly containing the elastomer layer ($E_L = 2.28$ N/mm^2, $\nu_L = 0.386$). To this end, two different discretization approaches are compared in a convergence study: Refinement of the mesh, as shown in Figure 3.5, without changing the polynomial order p (h-refinement) or increase of p in the in-plane directions from 2 to 8 while the mesh, depicted in Figure 3.2a, remains coarse (p-refinement). For each case, Figure 3.6 shows the relation between the number of unknowns and the root mean square error ε_f of the natural frequencies with respect to an overkill FE solution. It can be seen that the most efficient way is p-refinement. By applying this strategy, an ε_f of less than 1 % down to 0.24 % is reached with about 2.5 to 5 times fewer degrees of freedom than by using just quadratic elements. For example, if p is chosen between 2 and 4, an accurate solution with an error ε_f of 0.7 % is attained with only 1.7×10^4 degrees of freedom. The results demonstrate that the computational efficiency can be significantly increased by using high-order elements – in combination with an appropriate coarse mesh – instead of only linear or quadratic elements.

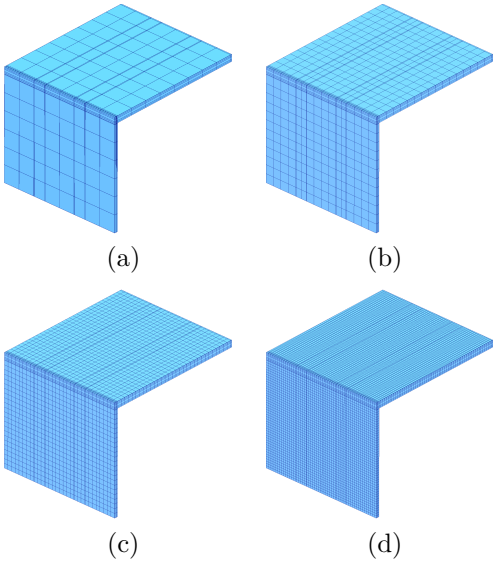

Figure 3.5: Meshes used for h-refinement: (a) mesh A, (b) mesh B, (c) mesh C, (d) mesh D, not illustrated: mesh E.[a]

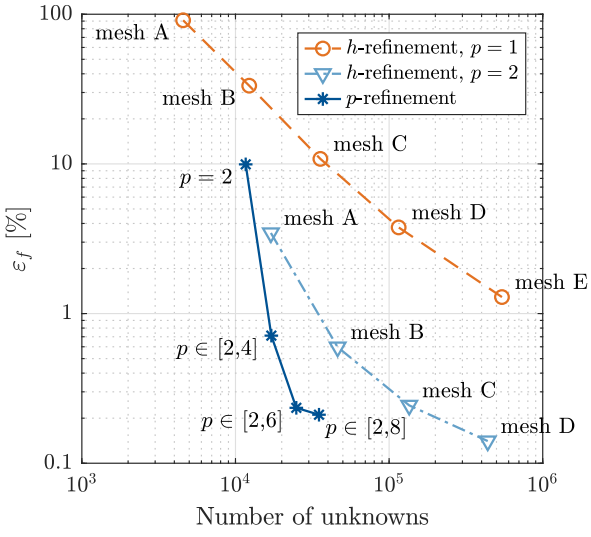

Figure 3.6: Relation between ε_f and the number of unknowns for different discretization approaches.[a]

3.1.4 Harmonic analysis

Apart from the natural modes, the frequency response functions served to validate the high-order FE model of the CLT assembly. To this end, a harmonic analysis was performed from 20 Hz to 150 Hz for each connection type and load case by solving Equation (2.31). For modeling the junction without elastomer, the Young's modulus E_L is set to 19 N/mm^2 and the Poisson's ratio ν_L to 0, whereas the junction with elastomer is considered by setting E_L to 2.28 N/mm^2 and ν_L to 0.386. A uniform loss factor of 2.2 % is applied, which was obtained from measurements [38]. Only to the finite elements representing the connection with elastomer, a different loss factor is assigned. It is based on the data sheet of the elastomer and rises in the considered frequency range from 10 % to nearly 21 % [46].

The simulations and the experimental tests were compared by means of the transfer accelerance, in the same way as described in [14]. For this purpose, the computed and measured absolute values of the transfer accelerance in out-of-plane direction were averaged over the measurement points of each component. The resulting mean absolute accelerances Y^{wall} and Y^{ceiling} for the case with elastomer under excitation of the wall are exemplarily shown in Figure 3.7. Computed and measured peak frequencies match well, which indicates that the density and stiffness parameters of the materials as well as the geometry and boundary conditions of the FE model are suitable. Since the peak values and width of the calculated mean absolute accelerance are mostly close to the measured ones, it can be concluded that also the loss factors are appropriate. In the frequency range over about 80 Hz, however, the measured and simulated mean absolute accelerances at

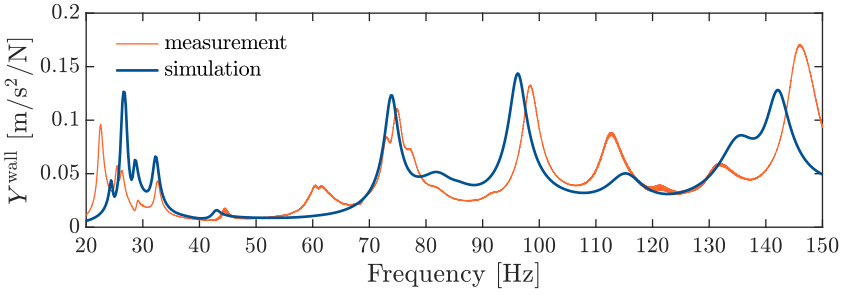

(a)

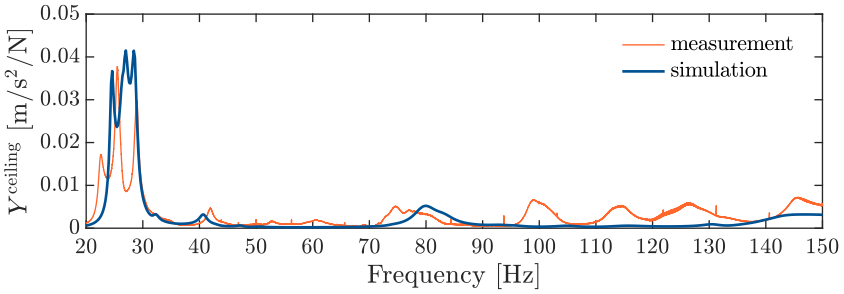

(b)

Figure 3.7: Mean absolute accelerances in out-of-plane direction for the case with elastomer under excitation of the ceiling at the measurement points of: (a) the wall, (b) the ceiling.[a]

the indirectly excited component partly differ. Accepting small differences between simulations and measurements, it follows that the presented model is suitable to predict the vibration behavior of the directly excited component up to about 150 Hz and of the indirectly excited component up to about 80 Hz. As shown in the following section, this model was used in Paper B to verify the mortar-based approach for representing elastomer layers.

3.2 Verification of the modified mortar formulation for elastomers [b]

Paper B introduces the modified mortar formulation, described in Section 2.4.2, for the case of isotropic viscoelastic layers. Moreover, the approach was verified and its accuracy was demonstrated therein based on two numerical examples. Both of them represent typical solid timber structures. One is an assembly of two components and the other a larger building part.

3.2.1 Wall and ceiling assembly

The first investigated structure consists of a single wall and a ceiling made of CLT and contains an elastomer layer between its components. It is identical to the test structure studied in Paper A. In this context, however, the validated conforming model is compared to a mortar-based one whose non-conforming mesh is shown in Figure 3.8. A time-harmonic excitation is applied on the ceiling, as depicted in Figure 3.9. The conforming model has 4.9×10^4 unknowns, whereas the mortar-based one exhibits only 2.5×10^4 unknowns.[1] In both models, the represented elastomer layer is 12.5 mm thick. The Young's modulus E_L is 2.28 N/mm^2, the Poisson's ratio ν_L is 0.386, and the loss factor η_L is frequency-dependent, starting from 10.0 % at 20 Hz and rising to 23.2 % at 200 Hz [46].

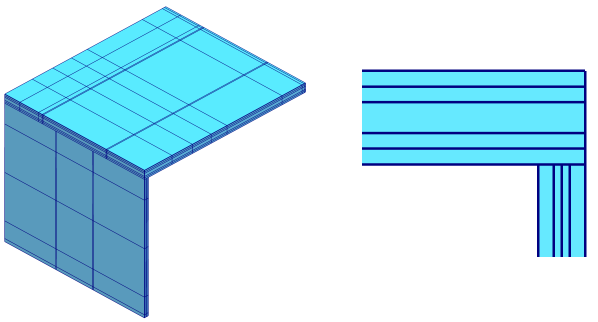

(a) (b)

Figure 3.8: Non-conforming mesh of the wall and ceiling assembly: (a) total view, (b) detail.[b]

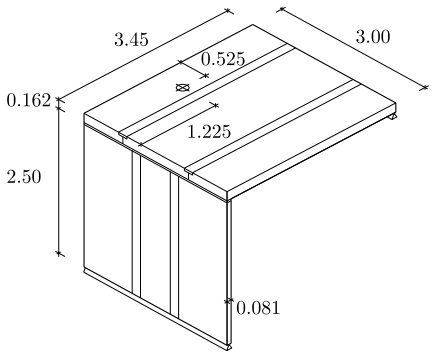

Figure 3.9: Excitation point of the wall and ceiling assembly [m].[b]

[1] In the harmonic analysis, the conforming model has more unknowns than in the modal analysis presented in Paper A (1.7×10^4 unknowns) because the problem is complex-valued and the associated mesh was adapted to capture the boundaries of the load surface by element edges.

Moreover, two additional cases are considered in order to investigate the influence of the elastomer layer and the robustness of the modified mortar method. In one case, the thickness of the elastomer is increased to 25 mm, and in the other case, η_L is reduced to 2.2 %, which is equal to the value assigned to the CLT components.

Figure 3.10 depicts the mean transfer accelerances Y^{dir} and Y^{ind} of the directly and the indirectly excited components computed by the conforming and the mortar-based model. To this end, 100×100 evaluation points were placed across the surface of each component. In addition, Y^{dir} and Y^{ind} were averaged over frequency bands with the upper limits of 50 Hz, 100 Hz, 150 Hz, and 200 Hz. The relative error $\delta_{Y,\mathrm{dir}}$ and $\delta_{Y,\mathrm{ind}}$ of the frequency-averaged transfer accelerances obtained from the mortar-based discretization with respect to the results of the conforming model are given in Table 3.1.

As can be seen in Figure 3.10, the loss factor of the elastomer η_L has a significant influence on the transfer accelerances. In each case, nevertheless, there is a good agreement between the results of the conforming and the mortar-based models. Not only the peak frequencies but also the maximum values and the width of the transfer accelerances computed with the mortar method are close to the ones determined with the conforming discretization. This is observed in the directly excited ceiling (Figure 3.10a) as well as in the indirectly excited wall (Figure 3.10b). The largest difference between the two models occurs at 79 Hz to 81 Hz, as shown in Figure 3.10b. A reason for the greater deviation might be that the respective resonant mode exhibits large deformations in the intermediate layer varying non-linearly in the thickness direction. These deformations cannot be represented exactly by the linear approach introduced in Equation (2.57). Nevertheless, relatively small deviations $\delta_{Y,\mathrm{dir}}$ and $\delta_{Y,\mathrm{ind}}$ being not greater than 6.17 % for $\eta_L \in [10\,\%, 23.2\,\%]$ and 7.30 % for $\eta_L = 2.2\,\%$ are obtained in all frequency bands in

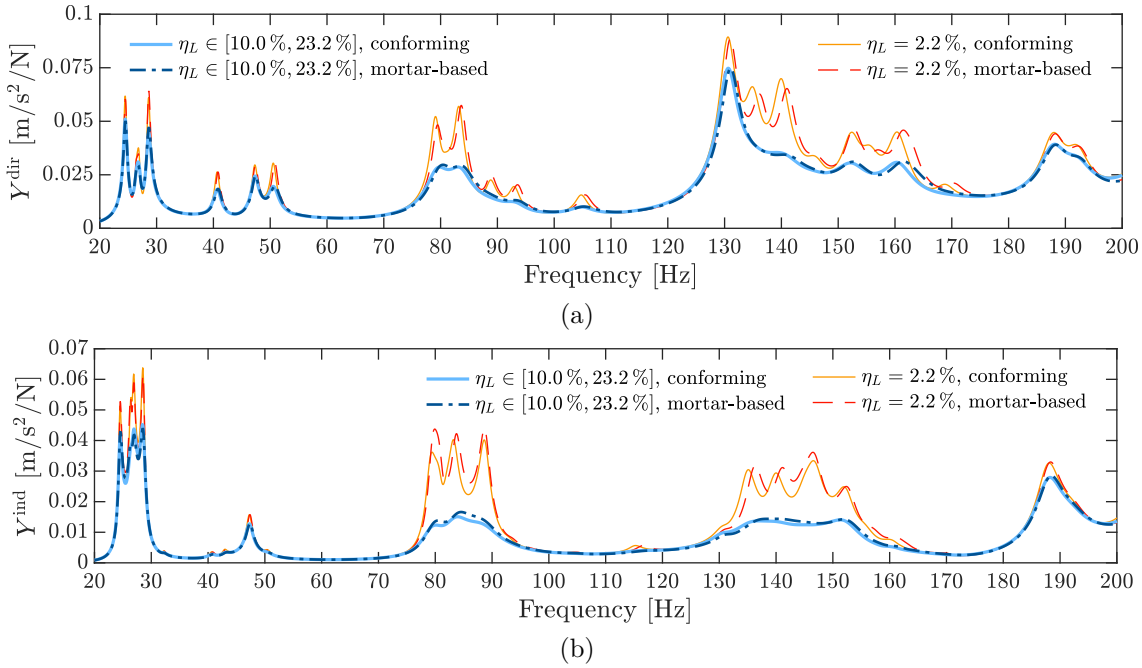

Figure 3.10: Mean absolute accelerances in the case of a 12.5 mm thick elastomer layer: (a) ceiling, (b) wall.[b]

Table 3.1: Relative deviations (single wall and ceiling assembly).[b]

	$b_L = 12.5\ mm$ $\eta_L \in [10.0\%, 23.2\%]$		$b_L = 12.5\ mm$ $\eta_L = 2.2\%$		$b_L = 25.0\ mm$ $\eta_L \in [10.0\%, 23.2\%]$	
frequency band [Hz]	$\delta_{Y,\mathrm{dir}}$ [%]	$\delta_{Y,\mathrm{ind}}$ [%]	$\delta_{Y,\mathrm{dir}}$ [%]	$\delta_{Y,\mathrm{ind}}$ [%]	$\delta_{Y,\mathrm{dir}}$ [%]	$\delta_{Y,\mathrm{ind}}$ [%]
20 Hz to 50 Hz	0.05	0.35	0.40	0.53	2.57	2.07
50 Hz to 100 Hz	3.34	6.17	2.21	7.30	10.05	10.41
100 Hz to 150 Hz	1.04	0.15	1.97	1.44	2.12	9.71
150 Hz to 200 Hz	1.38	1.97	2.34	2.18	3.54	2.21

the case of an elastomer thickness b_L of 12.5 mm (Table 3.1). Even if b_L is increased to 25 mm, the results of the mortar-based model match well with those of the conforming model. Here, the relative deviations are slightly higher with up to 10.41 %.

3.2.2 Building part

The second example is a more complex structure made of multiple cross-laminated timber components, which form a building part. The five walls are clamped at the bottom, and the ceiling is excited by a time-harmonic load. Between each wall and the ceiling, there is a 12.5 mm thick elastomer layer. In one model, the layers are represented by conforming hexahedral elements (Figure 3.11a) and, in the other, by the proposed mortar coupling (Figure 3.11b). The Young's modulus E_L is 3.37 N/mm^2, the Poisson's ratio ν_L is 0.42, and the loss factor η_L is 11.5 % at 20 Hz and increases to 27.6 % at 200 Hz [48]. As depicted in Figure 3.11, the layers of the cross-laminated timber components are not resolved individually by finite elements. Hence, the material parameters from Paper A were homogenized over the thickness of the components with the method presented in [49]. The polynomial orders of the elements are 4 and 5, leading to 2.0×10^5 unknowns in the conforming model and 1.3×10^5 unknowns in the mortar-based one.

The comparison is carried out in the same way as in the first example. Also in this

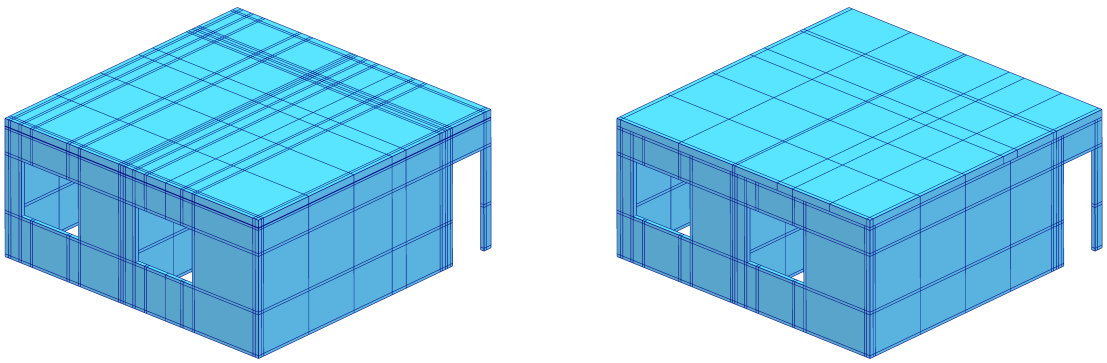

(a) (b)

Figure 3.11: FE meshes of the building part: (a) conforming, (b) non-conforming.[b]

more complex case, the results of the conforming and the mortar-based model agree well. The peak frequencies as well as the maximum values and width of the mean absolute accelerances obtained from these models are close to each other in each component. The relative error $\delta_{Y,\mathrm{dir}}$ determined for the directly excited ceiling is not greater than 3.6 % in all frequency bands, and the relative errors $\delta_{Y,\mathrm{ind\,1\text{-}5}}$ calculated for the indirectly excited walls are below 7.9 %. This shows that the vibration behavior of a complex elastomer bedded CLT structure can be accurately predicted with the modified mortar method.

3.3 Analysis of a multistory building [c]

Paper C integrates the mortar method into the digital planning process of solid timber buildings and demonstrates its significant advantages. In the presented approach, the structural components defined by a building information model are discretized separately such that mesh generation can be simplified and better adapted to the geometry. As the resulting meshes are non-matching, the mortar method is used to connect the components. In combination with higher-order finite elements, computationally efficient volumetric FE models for complete buildings can be automatically created in this way. To validate this modeling technique, it was applied to a test building, as shown in the following.

3.3.1 Test building and measurements

The investigated eight-story building is depicted in Figure 3.12. It is 23.9 m tall, and its base area is 10×20.4 m^2. The solid timber walls are partly made of vertical wooden blocks and partly of CLT panels, both of which are supplemented by gypsum fiberboards. The ceilings consist of CLT panels and additional layers. Their exact structure varies depending on the floor. The connections between the solid timber elements do not contain elastomers. Furthermore, there is a staircase core of 25 cm thick reinforced concrete walls, to which the solid wood elements are connected by angle joints.

Figure 3.12: Test building.[c]

The lowest natural frequencies of the building were determined in two independent measurements [50, 51]. In both investigations, a bending mode with displacements in the direction of the smaller building dimension (x-direction) was identified at 2.34 Hz [50] and 2.29 Hz [51], respectively. Moreover, vibrations in the x-direction and in the direction of the larger building dimension (y-direction) were detected in the range between 3.0 Hz and 3.4 Hz. In accordance with [51], it is assumed that the second natural frequency is 3.05 Hz and that the associated mode shape exhibits displacements in the x- and y-directions.

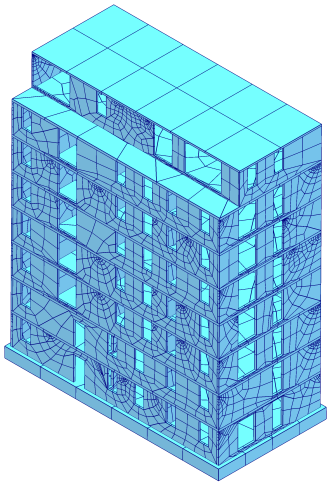

Figure 3.13: Non-conforming hexahedral FE mesh of the test building.[c]

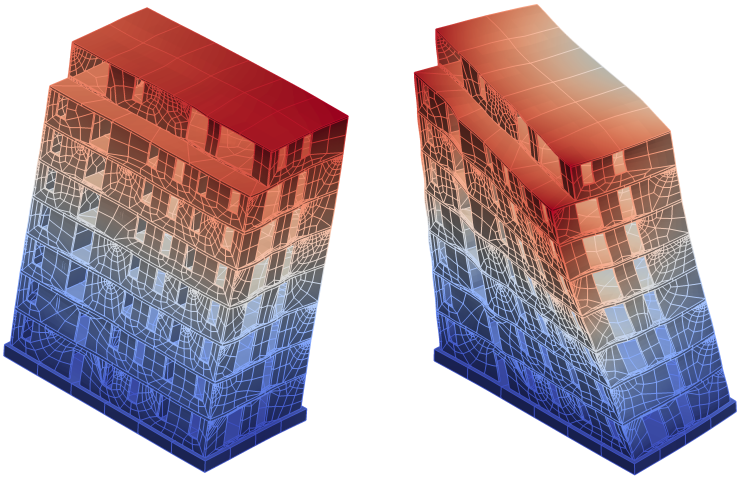

(a) (b)

Figure 3.14: Calculated mode shapes of the test building: (a) 2.16 Hz, (b) 3.11 Hz.[c]

3.3.2 Finite element model

The FE model of the test building, shown in Figure 3.13, comprises only 9286 hexahedral p-elements of order 3 and therefore has not more than 4.6×10^5 unknowns. This is achieved by discretizing the relevant structural components independently and by coupling them through the mortar method. Moreover, the layered structures of the solid timber walls and ceilings are homogenized based on the approaches described in [49] and [52]. It is assumed that the dynamic bedding module of the ground is 100 MN/m^3, as specified for pebbly coarse sand in [53], and that the connections of the components are rigid. Furthermore, the strength class of the timber is presumed to be C24 and the one of the concrete C30/37.

3.3.3 Results and discussion

The first and the second computed natural frequency of the building are 2.16 Hz and 3.11 Hz. This leads to a relative error with respect to the measurements of less than 6 %. Figure 3.14 shows the associated mode shapes. As observed in the experimental tests, the second mode shape exhibits displacements in both the x- and the y-direction due to the eccentrically located staircase core. Therefore, it can be concluded that the computations agree well with the measurements. Furthermore, the modeling costs are vastly reduced by the mortar-based approach, and high computational efficiency is obtained by the higher-order elements in combination with a relatively coarse mesh. The assumptions described above nevertheless need to be validated, particularly because a parameter study showed that the dynamic bedding module and the coupling rigidity between the components significantly influence the computational results.

The p-version of FEM and the modified mortar method have been successfully applied

to the analysis of solid timber structures. Numerical models of a representative CLT assembly were validated and verified in Papers A and B. Furthermore, Paper C demonstrates the increased modeling and simulation efficiency enabled by these discretization approaches. In the following chapters, which summarize Papers D and E, additive manufacturing is introduced as a further field of application. To this end, the current state of AM in construction with a focus on digital planning methods is first reviewed before the suitability of the modified mortar method – in combination with p-FEM and FCM – is investigated for AM structures.

Chapter 4

Additive Manufacturing in Construction [d]

AM techniques are used in various industries to create physical prototypes as well as end-use parts. In the construction sector, architectural models have been created with these methods for more than a decade. Furthermore, recent years have seen a vast increase in research on printing building components, and first construction projects have been implemented by large AM systems based on robotic arms or gantry robots [54–57]. This development can be attributed to the opportunities AM offers. AM allows building companies to produce geometrically complex structures, to vary materials within a component according to its functions, and to automate the construction process starting from a digital model. These advantages can be exploited if the building components and AM processes are modeled appropriately in the planning phase. To this end, several digital methods for designing printable parts and for planning AM processes have been developed. In addition, file formats to store and exchange the resulting data have emerged.

Paper D provides an overview of the current state of AM in construction. Processes, systems, and their applications are presented. Moreover, digital planning methods for 3D-printed building parts and AM processes are described.

4.1 Processes and applications

In AM processes, structures are made by joining materials, mostly layer by layer [58]. With regard to the printing of building parts, the research focus has been on concrete, metals, and polymers.

4.1.1 Concrete

The most important additive construction techniques for concrete are material extrusion and particle-bed processes:

- **Concrete extrusion.** After mixing, the fresh cementitious material is deposited through a nozzle along a defined path to create each layer. In order to ensure a good quality of the printed components, material and process parameters such as

the mix proportions and the addition of admixtures as well as the path and speed of the printing head need to be chosen properly and matched to each other [59–61]. Well-printed concrete can have similar strength and density in the hardened state as cast concrete [60]. In the last years, various extrusion processes were developed. An example is 3D Concrete Printing (3DCP) at Eindhoven University of Technology [62, 63], which is characterized by medium-fine filaments with cross-sectional dimensions up to several cm. By applying 3DCP, a bicycle bridge with a span of 6.5 m and a width of 3.5 m was constructed in the Netherlands. The superstructure of the bridge consists of elements that were printed within 48 h and assembled by post-tension tendons. In addition, reinforcement cables were embedded in some layers during their deposition [64].

- **Particle-bed processes.** In contrast to concrete extrusion processes, the raw materials are only brought together on the build platform. First, a layer of dry particles is created. Then, a fluid is deposited selectively to bond particles together in certain areas. This procedure is repeated until all layers are completed, each on top of one another. As the construction space needs to be completely filled with particles, it is more limited than in the case of concrete extrusion. However, particle-bed processes allow for more freedom of design due to the support from the non-bonded particles. Also, layer thicknesses down to 0.1 mm are possible such that small details can be printed with high accuracy. Furthermore, compressive strengths of over 70 MPa after 7 days were achieved in recent studies. An established particle bed system for large-scale applications is D-Shape, developed by Enrico Dini. It served, for example, to print a 12 m long and 1.75 m wide pedestrian bridge that was installed in Madrid [65, 66].

Concrete has in general a relatively low tensile strength and is quite brittle. Therefore, solutions for the integration of reinforcement have also been developed in the context of AM. They are reviewed in [67, 68] and can be categorized according to whether the reinforcement is external or internal and whether it is installed before, during, or after printing.

4.1.2 Metals

Steel and aluminum alloys can be printed using directed energy deposition and powder bed fusion processes:

- **Directed energy deposition.** A heat source such as a laser or an electron beam creates a melt pool on the surface of the workpiece. At the same time, metal powder or wire is added to the melt pool in order to generate an additional layer [69]. Directed energy deposition processes such as laser metal deposition (LMD) and wire arc additive manufacturing (WAAM) are relatively fast and well-suited for the production of large structures [70]. For instance, a 10 m long and 2.5 m wide stainless steel footbridge was printed by MX3D in the Netherlands [71].
- **Powder bed fusion.** In laser beam melting (LBM), electron beam melting (EBM), and direct metal laser sintering (DMLS), metal powder is spread across a work area and selectively fused by a laser or an electron beam to create a layer of the

final structure [69]. Powder bed fusion systems typically allow for high geometric accuracy and good mechanical properties, but they have a relatively low deposition rate and are mainly used to produce parts with small dimensions [72]. An example is a topologically optimized stainless steel node of a tensegrity structure that was designed and produced by Arup employing DMLS [73].

Very low porosity is needed for mechanical properties similar to those resulting from conventional production methods [69]. Therefore, the feedstock and the applied volume energy must be selected correctly. Furthermore, post-manufacturing treatments such as hot isostatic pressing, polishing, or chemical etching can reduce porosity and improve the surface quality [72].

4.1.3 Polymers

Applied methods to print polymer parts for buildings are material extrusion and powder bed fusion:

- **Polymer extrusion.** Several different 3D printers have been developed to create large-scale structures by extruding polymers [56, 74]. Among them are the C-Fab printer by Branch Technology [75], the KamerMaker by DUS Architects [76], and the Big Area Additive Manufacturing (BAAM) system by Oak Ridge National Laboratory [77]. In the BAAM system, a single screw extruder heats up a pelletized thermoplastic feedstock and deposits the melted material along the tool path. By using pellets instead of filaments, the deposition rate was significantly increased while reducing the feedstock costs [77]. For showcasing, the envelope of a cylindrical single-floored building with a ground area of 19.5 m^2 and a height of 2.8 m was printed by BAAM [78].
- **Powder bed fusion.** In selective laser sintering (SLS), layers of polymer powder are successively applied on top of each other. Between each step, a laser heats up the polymer particles in certain areas of the respective layer such that they are fused together. Benefits of SLS are the high resolution and quality which can be achieved, but it is more expensive and slower than material extrusion processes [72]. SLS was applied by Skanska and 3D Systems to produce geometrically complex polymer cladding for welded steel nodes of a roof structure in London. The 3D-printed covering does not have a structural function, but it was added for aesthetics and is resistant to rain, sunlight, and heat [79, 80].

Most pure polymers have only low stiffness and strength. However, polymer composites with improved mechanical properties, such as carbon fiber reinforced acrylonitrile butadiene styrene (CF-ABS), have been developed and used for AM [57, 72, 81, 77]. Moreover, polymer parts can be combined with steel or concrete components for load-bearing purposes.

4.2 Digital planning methods

The digital workflow to generate the instructions for 3D printers starts off by creating a computer-aided design (CAD) model of the object. In this step, numerical methods can

support form-finding and dimensioning. For example, topology optimization allows generating lightweight structures with great performance by exploiting the increased design freedom AM offers [82, 73]. Aspects related to AM such as support structures, minimum length scales, material anisotropy, and multiple scales can also be considered during the optimization [83]. After the design phase, the CAD model is converted into a form suitable for planning the AM process. At present, the stereolithography (STL) file format, which only requires a surface triangulation, is most widely used [84]. In the process planning phase, the converted geometric model of the part is positioned and oriented in the build space, supplemented by support structures (if necessary), and sliced. Then, the tool path is generated and the process parameters are selected before they are finally translated to a machine language such as G-Code in order to numerically control the printer [85].

STL files describe AM parts by their surface using planar triangular facets. Because of their simple structure, the files can be easily created and read. However, they are only able to include geometry information and to represent an approximation of the CAD model. Furthermore, they are prone to flaws, including gaps and overlaps. Alternative formats such as AMF, 3MF, STEP, and IFC offer a more detailed and reliable data exchange than STL [86]. The Industry Foundation Classes (IFC) is standardized in ISO 16739 and provides a vendor-neutral exchange of BIM data [87]. It is generally considered the most promising format in this context because it has the potential to fully integrate the planning workflow for AM into the BIM method.

4.2.1 Building Information Modeling

A Building Information Model is a comprehensive digital representation of a building that contains geometric and semantic data, such as building element types and material properties. Since this data is interlinked, many planning processes can be automated to a high degree. Examples are quantity assessments, collision checks, as well as the generation of simulation models or construction plans [88]. Thus, BIM can significantly improve the planning quality and efficiency, not only for conventionally but also for additively manufactured building components. However, the integration of AM parts into Building Information Models without design restrictions imposes high demands on the geometric and material representation. Fortunately, various techniques have been developed that allow modeling almost any printable part, such as a cellular structure or an FGM object [89–92, 5]. The geometry of a solid body can be described in the following ways:

- **Boundary representation (B-rep).** In B-rep approaches, the surface is explicitly modeled, for example, by polygonal meshes or bivariate NURBS patches [89].
- **Volume representation (V-rep).** In V-rep techniques, the volume is explicitly represented using, for example, voxels, polyhedral meshes, trivariate NURBS patches [93, 94], Constructive Solid Geometry (CSG), or extensions of CSG [28, 89].

Furthermore, material distributions can be defined based on the respective geometric model or on geometry-independent functions that refer to specific coordinate systems or control features. Each of these methods has specific advantages and disadvantages such that they are suitable for different use cases [5].

With IFC, several geometry descriptions, such as a CSG model and a B-rep model consisting of NURBS surfaces, can be related to a building element. It is also possible to define a triangulated model based on a list of points. Moreover, building elements composed of multiple materials can be described as well [88]. However, in the present standardized version, an explicit description of volumetric information in the form of voxel models, polyhedral meshes, or trivariate NURBS patches cannot be directly made with IFC objects. Also, the possibility of representing graded material in IFC files by various types of material distribution functions needs to be developed and implemented. Apart from that, IFC should provide data for process planning to further integrate AM and BIM. For example, in the context of concrete extrusion, Davtalab et al. [95] suggested to extend Building Information Models by additional parameters for the print material and the construction robot.

4.2.2 Structural verification

The planning procedure and thus the quality of AM parts can be significantly enhanced by structural verifications based on numerical simulations of the printing process and of the final state:

- **Verification of AM processes.** Failures and large deformations can be prevented by better adapting the part orientation, support structures, and process parameters to the specific conditions of each printing process. Furthermore, distortions can be compensated by the input geometry. To this end, methods to simulate AM processes for concrete [96, 97], metal [98–103], and polymers [104–109] are being developed. Additionally, researchers strive to predict product properties such as strength and fatigue resistance [110]. The aim is to provide data for the verification of built-in AM parts and to optimize AM processes with regard to the part performance. A major challenge is, however, the development of a comprehensive understanding of the multiscale and multiphysics mechanisms in AM processes. Moreover, the computational costs of detailed simulations are very large, there is a multitude of interacting factors, and it is difficult to carry out validations, especially at small scales [110, 98].
- **Verification of built-in AM parts.** If a building part has a load-transferring function, its stability and serviceability, including the limitation of deformations, need to be ensured. Therefore, the respective material and failure behavior in the final state must be known. Experimental data has been used to develop the design and verification procedures for conventionally produced components defined in technical codes. For AM parts, such procedures still have to be developed. The structural behavior of additively manufactured specimens, which depends on the raw material and the printing process, was experimentally studied and reviewed for concrete printing in [60, 111–116], for metal AM in [117, 118, 69], and for polymer extrusion-based AM in [77, 81]. Moreover, FE models of 3D-printed parts were analyzed and compared to measurements in [119–124]. For example, metal AM lattice structures were investigated in [120–122]. The simulations of the lattice structures showed a satisfactory to excellent agreement with the measurements, but only if the process-induced defects were considered. Despite these studies, there is

a significant lack of experimental data and validated models for printed building components [62, 117, 125]. This is a major obstacle for establishing computation-based proofs of stability and serviceability.

Challenges for numerical simulations also arise from the design freedom AM offers because parts can be printed that exhibit complex geometries and small features down to 0.1 mm or even less. Therefore, the following chapter presents an efficient multiscale simulation approach based on FCM and the modified mortar method.

Chapter 5

Multiscale analysis of periodic microstructures [e]

Polymers such as polyurethane elastomers are often used for vibration reduction due to their high loss factors. As shown in Chapter 3, they can be placed in the form of damping layers in between structural parts for this purpose. However, their relatively small stiffness can lead to even larger vibrations in directly excited components [126]. Alternatively, stiff materials with relatively high loss factors can be employed. Examples are high damping metals [127, 128] and aluminum metal matrix composites [129, 130]. Moreover, designs for AM microstructures have been developed in recent years [3, 131]. For instance, Andreasen et al. [3] identified two-phase microstructures with high stiffness and optimized damping properties. They can be produced by additively manufacturing stiff lattice structures and injecting damping material into the cavities. Predicting the mechanical behavior of parts made from such microstructures can, however, require high modeling and computational effort because of their multiscale nature and potentially complex geometry.

Paper E presents a simulation framework to investigate the vibration behavior of complex multiscale structures. Therein, the effective material parameters of the respective microstructure are obtained from computational homogenization and employed in large-scale simulation models based on the modified mortar method. The main contributions of Paper E are: (a) The use of an embedded domain method (FCM) to numerically homogenize viscoelastic composite microstructures. (b) The application and verification of the modified mortar method to represent damping layers made of such structures. (c) Numerical studies on high-performance composites demonstrating the efficiency of the proposed multiscale approach.

5.1 Computational homogenization study

5.1.1 Unit cell design

The investigated composite microstructures consist of the unit cells shown in Figures 5.1 and 5.2, which are inspired by the topology optimization results of Andreasen et al. [3]. They are referred to as *octahedral* and *cubic* microstructure. Two geometric parameters are defined: the thickness of the struts connecting the stiff inclusions a_{strut} and the size

of the gaps filled with damping material a_{gap}, both of which are normalized to the unit cell size and set to 0.2 unless otherwise stated.

The constituents are considered isotropic and linear viscoelastic with a complex Young's modulus and a real Poisson's ratio. The parameter values of the stiff material are based on measurements of steel specimens [132–137] and those of the damping material on studies of polymethyl methacrylate (PMMA) [138, 139]. The storage Young's modulus of the stiff material E'_s is 180 GPa, and its loss factor η_s is 0.0025. The damping material parameters, in contrast, depend on the frequency: E'_d increases from 3.5 GPa to 5 GPa and η_d decreases from 0.08 to 0.05 with rising frequency from 1 Hz to 1000 Hz. Thus, PMMA offers a combination of a relatively high storage Young's modulus and loss factor compared to other pure polymers.

5.1.2 Homogenization and discretization approaches

The composite microstructures can be represented on the macroscale by a homogeneous linear viscoelastic material if the respective unit cells are much smaller than the overall structure. To obtain the associated effective constitutive matrices, computational homogenization is applied [3, 140]. Furthermore, as the microstructures are cubic symmetric, three complex effective material parameters are determined from each constitutive matrix [20]:

$$E_c = E'_c(1 + i\eta_{E_c}) \tag{5.1}$$

$$\nu_c = \nu'(1 + i\eta_{\nu_c}) \tag{5.2}$$

$$G_c = G'_c(1 + i\eta_{G_c}) \tag{5.3}$$

where E'_c, ν'_c, and G'_c are the effective storage Young's modulus, Poisson's ratio, and shear modulus, while η_{E_c}, η_{ν_c}, and η_{G_c} are the corresponding loss factors.

Numerical models of the unit cells were created to perform the computational homogenization study. The unit cell domain of the octahedral microstructure is described with a parametric CSG model and discretized on that basis using FCM [28]. For each material of the octahedral microstructure, a non-boundary-fitting FCM mesh is generated, as shown in Figure 5.3. The meshes are weakly coupled at the material interface by means of the penalty method [29]. This approach allows for an automated modeling procedure despite

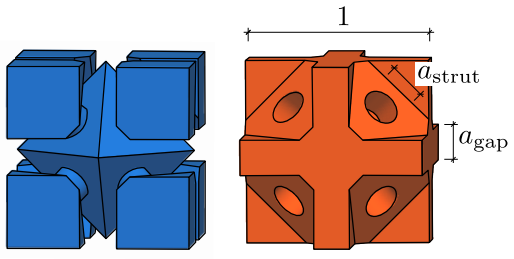

Figure 5.1: Unit cell of the *octahedral* microstructure: (a) stiff material, (b) damping material.[e]

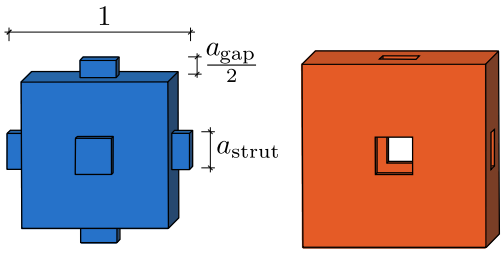

Figure 5.2: Unit cell of the *cubic* microstructure: (a) stiff material, (b) damping material.[e]

the geometric complexity of the microstructure. By contrast, the cubic microstructure is discretized with a conforming FE mesh, depicted in Figure 5.4, due to the simplicity of its geometry. The polynomial degree p of the shape functions is chosen based on a convergence study. It is set to 3 in the case of the octahedral microstructure and to 4 in the case of the cubic microstructure, leading to a relative error of the effective material parameters of less than 3.2 % with respect to an overkill solution.

5.1.3 Results and discussion

The octahedral and the cubic microstructure exhibit large stiffness and good damping properties in the frequency band from 1 Hz to 1000 Hz. The storage Young's modulus E_c' ranges from 27 GPa to 39 GPa, which is more than 15 % of the stiff material parameter E_s', and the loss factor η_{E_c} ranges from 0.035 to 0.024, which is more than 40 % of the damping material parameter η_{E_d}. A significant difference between the octahedral and the cubic microstructure is found with respect to the shear modulus. Namely, the octahedral microstructure has a considerably higher G_c' and lower η_{G_c} than the cubic microstructure.

The parameters defining the geometry and material of the octahedral microstructures were, moreover, individually varied from their original values in order to investigate their influence on the effective material properties. The geometric parameters a_{strut} and a_{gap} were varied between 0.1 and 0.3. The results show that the storage Young's modulus E_c' can be increased by two measures: raising the strut thickness a_{strut} or lowering the gap size a_{gap}. In contrast to the latter measure, a larger strut thickness a_{strut} unfortunately results in a significantly lower loss factor η_{E_c} as well. The impact of the stiff and the damping material parameters is shown in Figure 5.5. To this end, a parameter study was conducted where the material parameters were multiplied one at a time by a variation factor ranging from 0.025 to 2. The graphs specify the factors by which E_c' and η_{E_c} change in each case. E_c' rises with increasing storage Young's moduli of both constituents and η_{E_c} rises with increasing loss factors. Unlike the loss factor of the damping material η_d, however, the one of the stiff material η_s has almost no effect. Furthermore, the storage Young's moduli E_s and E_d considerably influence the effective loss factor η_{E_c}. Particular attention should be given to the drastic decline of η_{E_c} if E_d falls below a certain value. Therefore, polymers with very low stiffness should be avoided here, even if they exhibit high loss factors. Instead, it can be beneficial – not only for the stiffness but also for the damping properties of the composite – to select a polymer with a storage Young's modulus greater than 1 GPa within the relevant frequency and temperature range.

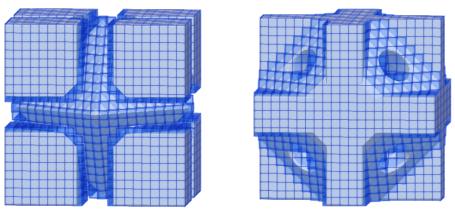

(a) (b)

Figure 5.3: FCM meshes for the octahedral microstructure: (a) stiff, (b) damping material.[e]

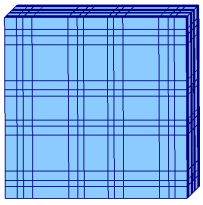

Figure 5.4: Boundary-conforming FE mesh for the cubic microstructure.[e]

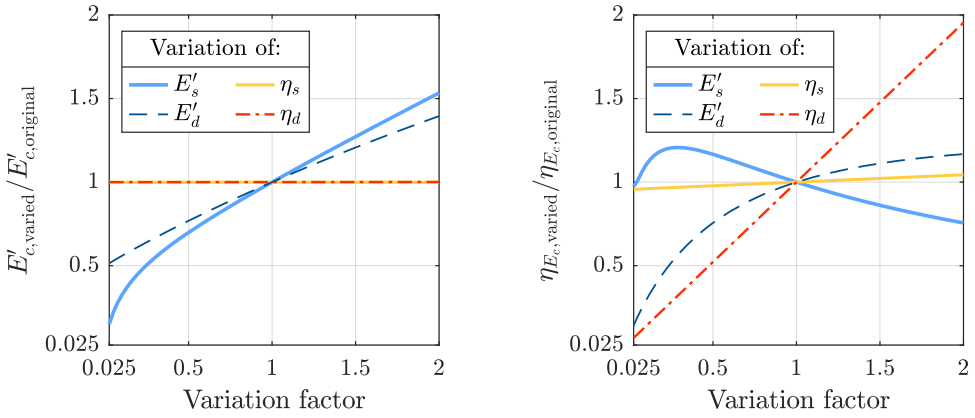

Figure 5.5: Change of the effective material parameters E'_c and η_{E_c} of the octahedral microstructure due to a variation of the stiff and the damping material parameters from their original values at 10 Hz: $E_s = 180$ GPa, $\eta_s = 0.0025$, $E_d = 4$ GPa, $\eta_d = 0.07$.[e]

5.2 Verification of the modified mortar formulation for periodic microstructures

After introducing the modified mortar method in Paper B for isotropic elastomer layers, it was extended in Paper E to layers made of cubic symmetric microstructures and applied to the following example for verification.

5.2.1 Test structure

The assembly depicted in Figure 5.6 consists of a vertical and a horizontal steel bar whose dimensions are $36 \times 9 \times 2000$ mm^3 and $1600 \times 9 \times 72$ mm^3. They have the same material parameters as the stiff constituent of the composite microstructures described above. The connection between the bars contains a damping layer made of one of the microstructures. Unless otherwise stated, it has a thickness b_L of 18 mm. Also, the case of a rigid connection without a damping layer is considered. It is used as a reference to evaluate the impact of the layer. The vertical beam is clamped to the ground, whereas the horizontal one is directly excited by a time-harmonic load oriented in z-direction. Two symmetry boundary conditions are applied such that the structure is actually a frame comprised of components whose dimensions in the y-direction are twice as large as indicated.

5.2.2 Numerical models

Based on the effective material parameters calculated in Section 5.1, the heterogeneous damping layer of the test structure is represented in two different ways. In the conforming FE model (Figure 5.7a), it is explicitly resolved by a high-order finite element and, in the mortar-based FE model (Figure 5.7b), it is taken into account by the modified mortar coupling. Both the conforming and the mortar-based models use hexahedral p-elements of order 9 with large aspect ratios [6]. Compared to an overkill solution, the root mean

square error of the natural frequencies up to 900 Hz is less than 0.1 % in the case of the conforming model and less than 0.2 % in the case of the mortar-based model.

Moreover, numerical models of the assembly fully resolving the octahedral and the cubic microstructure of the damping layer are analyzed (Figure 5.8). They serve as a reference to verify the homogenization approach. In these models, the damping layer consists of $4 \times 1 \times 2$ unit cells, each discretized in the same way as described in Section 5.1.2. This leads to 5.0×10^6 unknowns in the case of the octahedral microstructure and 1.5×10^6 in the case of the cubic microstructure. By contrast, the conforming model employing the effective material parameters has only 10 432 unknowns and the mortar-based one 8 968.

5.2.3 Results and discussion

The vibration behavior of the test structure subjected to the given time-harmonic load was studied in a frequency response analysis. Therein, the mean accelerances Y^{dir} and Y^{ind} were calculated by averaging the transfer accelerance over 100 evenly distributed evaluation points along the longitudinal axis of the directly and the indirectly excited bar, respectively. Figure 5.9 shows Y^{dir} and Y^{ind} from 140 Hz to 150 Hz for the cases with and without a damping layer. The layer is made of the standard octahedral microstructure described in Section 5.1.1 and represented in different ways using the numerical models presented above. It can be seen in Figure 5.9 that the damping layer has a significant effect on the vibration behavior of the test structure. Compared to the case of a rigid connection without a damping layer, the peak value of the mean accelerance Y^{dir} is reduced by 20.6 % and that of Y^{ind} by 39.2 %. Furthermore, the fully resolved and the homogenized damping layers lead to matching results. The peak accelerances differ by less than 6.9 % and the

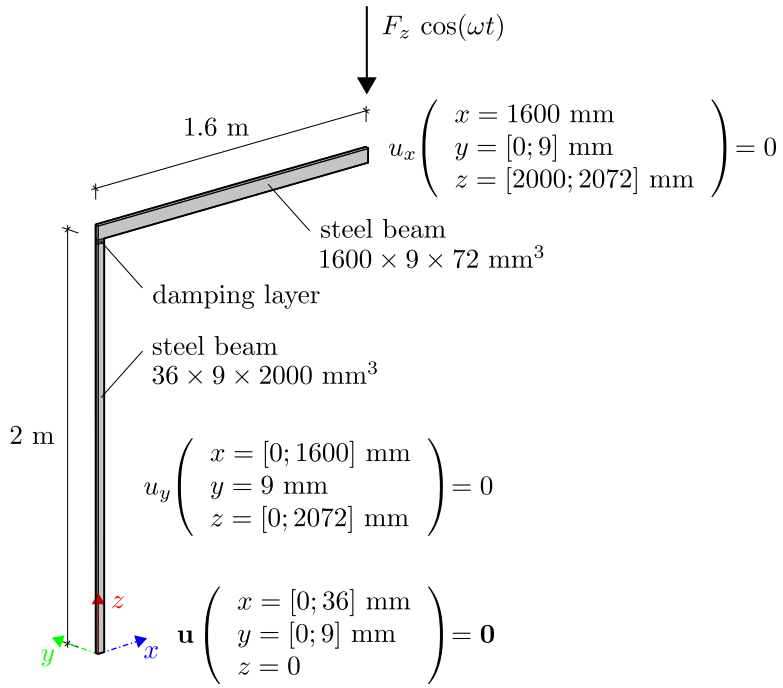

Figure 5.6: Dimensions and boundary conditions of the test structure.[e]

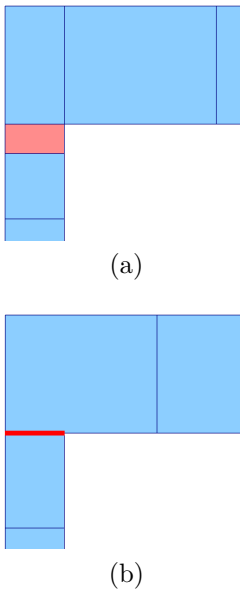

Figure 5.7: FE meshes of the test structure: (a) conforming, (b) non-conforming.[e]

peak frequencies only by at most 1.05 %. A similar outcome is obtained for the cubic microstructure. This indicates that the effective material parameters and the modified mortar coupling are well suited for the considered use case.

These findings are consistent with a more extensive investigation in which several different conforming and mortar-based models were compared in a wider frequency range from 0.1 Hz to 900 Hz. The results show that the damping layer reduces the peak accelerances on average by around 27.2 % if a_{strut} is 0.2 and by around 36.8 % if a_{strut} is 0.1, regardless of whether the octahedral or the cubic microstructure is used. Furthermore, the vibrations of the directly and the indirectly excited component are reduced to a similar extent, which can be most likely attributed to the high stiffness of the microstructures impeding considerable elastic insulation. The relative error of the peak accelerances obtained from the mortar-based model with respect to those of the conforming one is on average less than 7.2 % in the directly excited component and not greater than 5.8 % in the indirectly excited one. This confirms not only the accuracy but also the robustness of the modified mortar method because the analysis was performed for multiple microstructures and different layer thicknesses.

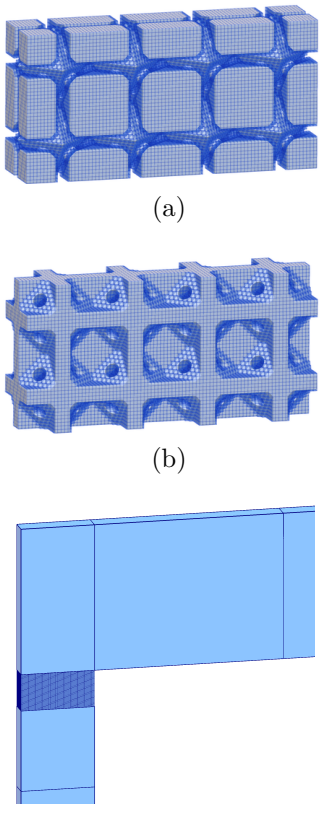

(a) (b) (c)

Figure 5.8: Non-boundary-fitting FCM meshes of the fully resolved octahedral microstructure: (a) stiff constituent, (b) damping constituent, (c) combined meshes.[e]

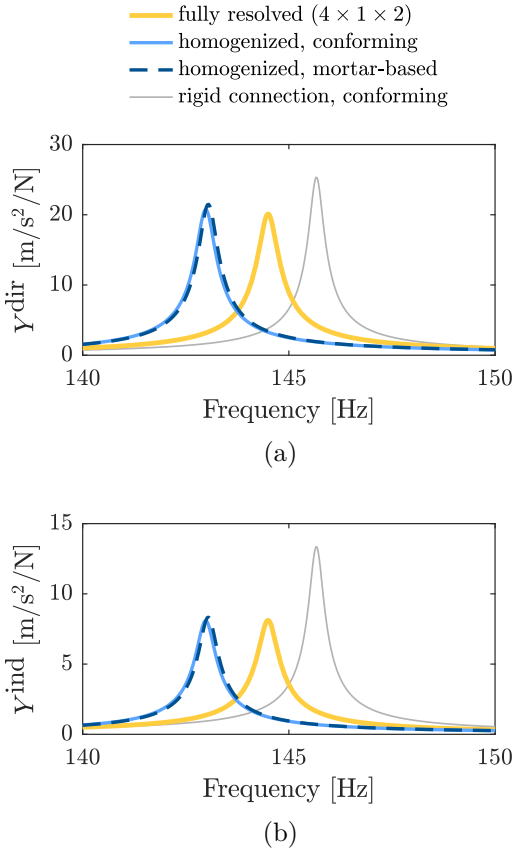

Figure 5.9: Mean accelerances Y^{dir} and Y^{ind} for various representations of the octahedral microstructure: (a) directly excited component, (b) indirectly excited component.[e]

Chapter 6

Conclusion

The research presented in this thesis focuses on vibration analysis of complex structures assembled from multiple components. In the proposed approach, the structural parts are discretized separately using high-order finite elements. The non-matching meshes are then weakly coupled by the mortar method. This allows for a simplified modeling procedure as well as for computationally efficient simulations. For example, the meshes can be better adapted to the part geometries, and hexahedral mesh generation can be automated for complete buildings. Moreover, different discretization approaches, such as p-FEM and FCM, can be combined by applying the mortar method. In order to further increase the efficiency of the modeling and simulation process, the mortar method was modified in this work to represent linear viscoelastic layers between the weakly coupled components in a dimensionally reduced way. By this means, thin damping layers, which can have a significant effect on the vibrations of the entire structure, do not need to be discretized explicitly with finite elements. Instead, they can be easily taken into account by a weak coupling condition. This approach was verified for two challenging application fields, namely, cross-laminated timber construction and additive manufacturing:

- **Cross-laminated timber** offers great benefits, such as biaxial load transfer, higher heat storage capacity than timber frame modules, and less weight than reinforced concrete. However, to predict the vibrations of CLT assemblies, the components and connections need to be modeled appropriately. Motivated by that, a high-order FE model for CLT assemblies based on a conforming mesh was developed and validated by measurements for the cases with and without elastomer layers between the components. In this context, it was demonstrated that the high-order approach significantly increases the numerical efficiency. Furthermore, it was shown that the material values of the elastomer determined by the technique of Negreira et al. [22] are suitable to represent the screw connection with elastomer layer. On this basis, the modified mortar method was verified by numerical examples of CLT assemblies. The comparisons between the conforming and the mortar-based models show good accordance for different material values and thicknesses of the elastomer layer. Finally, the advantages and suitability of integrating the mortar-based approach into the planning process of construction projects were demonstrated using the example of an existing multistory building made of solid timber components. Computations and measurements of the two lowest natural frequencies and associated mode shapes

agreed well, while the modeling and computational costs were small.
In the scope of this thesis, the representation of a connection between a CLT wall and ceiling with and without an elastomer layer was thoroughly studied and validated in the range from 20 Hz to 150 Hz. Future investigations could include further types of connections in a wider frequency range because the quality of their representation can significantly influence the computed natural frequencies of solid timber assemblies and buildings.

- **Additive manufacturing** is being investigated intensively by research institutes and companies for use in the construction industry and has even been applied to first building projects in recent years. For this purpose, large AM systems based on robotic arms or gantry robots as well as printing processes for concrete, metals, and polymers have been developed. In comparison to many conventional construction methods, AM offers considerable benefits. For example, it can automate the complete production process and provide building parts that exhibit complex geometries and material distributions. However, suitable digital planning methods and their integration into the BIM method are needed to fully exploit these advantages in the construction sector. To this end, the vendor-neutral file format IFC should be extended by different V-rep models, material distribution functions, and process planning information. Apart from a comprehensive file format to exchange relevant data for AM, structural verification procedures based on numerical simulations of the printing process and of the final state should be further improved in order to prevent failures and large deformations. Despite significant progress in this field, validated models for final AM parts as well as an in-depth understanding of the multiscale and multiphysics mechanisms in AM processes still need to be developed. Additionally, the large design freedom of AM, which allows for complex geometries and small features, can lead to considerable difficulties for numerical modeling and simulation.
  Heterogeneous composites producible by AM can be designed in a way such that they exhibit high stiffness and good damping properties. Therefore, a mortar-based simulation framework to investigate the vibration behavior of assemblies containing these structures as damping layers was developed in the scope of this work. It starts by homogenizing the composite microstructures with FCM, followed by the assignment of the effective material parameters to mortar interfaces that represent the respective damping layers in large-scale simulation models. The efficiency of this approach was demonstrated in numerical studies on exemplary high damping composites, each consisting of a stiff and a damping constituent. The studies also revealed that a higher Young's modulus of the damping material significantly increases both the stiffness and the damping capacity of the composites. Furthermore, large-scale simulations in which the effective material parameters were employed for a damping layer showed a good agreement between conforming and mortar-based models for various composite designs and layer thicknesses. In addition, the homogenization approach was verified by simulation models that fully resolve the microstructure of the damping layer.
  The computational results should be validated by measurements on 3D-printed spec-

imens in future work. In this context, the presented framework could also be used to analyze the as-built structures instead of the original designs by performing the simulations on CT images. Also other aspects such as strength and fatigue life should be investigated, both numerically and experimentally. Moreover, other parts than damping layers can be made of the investigated composites, potentially in the form of functionally graded materials.

In this thesis, the modified mortar method was developed and successfully used to represent damping layers made of elastomers and heterogeneous composite materials in frequency response analyses. Further applications can be covered in future work. For example, the formulation can be adapted to nonlinear transient problems by employing a time-dependent constitutive equation. Moreover, the accuracy of the method could be further increased by introducing a higher-order approach for the displacements along the thickness direction of the layer.

Bibliography

[1] A. Rabold. *Anwendung der Finite Element Methode auf die Trittschallberechnung*. PhD thesis, Technische Universität München, 2010.

[2] R. Brandner, G. Flatscher, A. Ringhofer, G. Schickhofer, and A. Thiel. Cross laminated timber (CLT): Overview and development. *European Journal of Wood and Wood Products*, 74(3):331–351, 2016.

[3] C.S. Andreasen, E. Andreassen, J.Sø. Jensen, and O. Sigmund. On the realization of the bulk modulus bounds for two-phase viscoelastic composites. *Journal of the Mechanics and Physics of Solids*, 63(1):228–241, 2014.

[4] Y. Tang and Y.F. Zhao. A survey of the design methods for additive manufacturing to improve functional performance. *Rapid Prototyping Journal*, 22(3):569–590, 2016.

[5] B. Zhang, P. Jaiswal, R. Rai, and S. Nelaturi. Additive Manufacturing of Functionally Graded Material Objects: A Review. *Journal of Computing and Information Science in Engineering*, 18(4), 2018.

[6] A. Düster, E. Rank, and B. Szabó. The p-Version of the Finite Element and Finite Cell Methods. In E. Stein, R. Borst, and T.J.R. Hughes, editors, *Encyclopedia of Computational Mechanics Second Edition*, pages 1–35. 2017.

[7] J. Parvizian, A. Düster, and E. Rank. Finite cell method: h- and p-extension for embedded domain problems in solid mechanics. *Computational Mechanics*, 41(1): 121–133, 2007.

[8] B. Wassermann, S. Kollmannsberger, S. Yin, L. Kudela, and E. Rank. Integrating CAD and numerical analysis: 'Dirty geometry' handling using the Finite Cell Method. *Computer Methods in Applied Mechanics and Engineering*, 351:808–835, 2019.

[9] F. Ben Belgacem. The Mortar finite element method with Lagrange multipliers. *Numerische Mathematik*, 84(2):173–197, 1999.

[10] F. Casadei, E. Gabellini, G. Fotia, F. Maggio, and A. Quarteroni. A mortar spectral/finite element method for complex 2D and 3D elastodynamic problems. *Computer Methods in Applied Mechanics and Engineering*, 191(45):5119–5148, 2002.

[11] O.C. Zienkiewicz, R.L. Taylor, and J.Z. Zhu. Multidomain Mixed Approximations. In *The Finite Element Method: its Basis and Fundamentals (Seventh Edition)*, pages 361 – 378. Butterworth-Heinemann, Oxford, 2013.

[12] A. Boström, P. Bövik, and P. Olsson. A comparison of exact first order and spring boundary conditions for scattering by thin layers. *Journal of Nondestructive Evaluation*, 11(3-4):175–184, 1992.

[13] D.Z. Bare, J. Orlik, and G. Panasenko. Asymptotic dimension reduction of a Robin-type elasticity boundary value problem in thin beams. *Applicable Analysis*, 93(6): 1217–1238, 2014.

[14] Å. Bolmsvik, A. Linderholt, A. Brandt, and T. Ekevid. FE modelling of light weight wooden assemblies – Parameter study and comparison between analyses and experiments. *Engineering Structures*, 73:125–142, 2014.

[15] Å. Bolmsvik and A. Linderholt. Damping elastomers for wooden constructions – Dynamic properties. *Wood Material Science & Engineering*, 10(3):245–255, 2015.

[16] O. Flodén, G. Sandberg, and K. Persson. Reduced order modelling of elastomeric vibration isolators in dynamic substructuring. *Engineering Structures*, 155:102–114, 2018.

[17] T. Horger, S. Kollmannsberger, F. Frischmann, E. Rank, and B. Wohlmuth. A new mortar formulation for modeling elastomer bedded structures with modal-analysis in 3D. *Advanced Modeling and Simulation in Engineering Sciences*, 1:18, 2014.

[18] Klaus Jürgen Bathe. *Finite Element Procedures*. Prentice Hall, New Jersey, 2007.

[19] O. Rand and V. Rovenski. *Analytical methods in anisotropic elasticity: With symbolic computational tools*. Birkhauser Boston, 2005.

[20] Radovitzky, R. Module 3: Constitutive Equations. Lecture notes in 16.20 Structural Mechanics, Massachusetts Institute of Technology, Cambridge, Massachusetts, United States, 2013.

[21] J.J. Wijker. *Mechanical Vibrations in Spacecraft Design*. Springer-Verlag Berlin Heidelberg, 2004.

[22] J. Negreira, P. Austrell, O. Flodén, and D. Bard. Characterisation of an elastomer for noise and vibration insulation in lightweight timber buildings. *Building Acoustics*, 21(4):251–276, 2014.

[23] L. Cremer and M. Heckl. *Structure-Borne Sound*. Springer Berlin Heidelberg, 1988.

[24] B.C. Chakraborty and D. Ratna. *Polymers for Vibration Damping Applications*. Elsevier, Amsterdam, 2020.

[25] D. Roylance. Engineering viscoelasticity. Lecture notes in 3.11 Mechanics of Materials, Massachusetts Institute of Technology, Cambridge, Massachusetts, United States, 2001.

[26] B. Szabó and I. Babuška. *Finite Element Analysis*. John Wiley & Sons, New York, 1991.

[27] A. Düster, H. Bröker, and E. Rank. The *p*-version of the finite element method for three-dimensional curved thin walled structures. *International Journal for Numerical Methods in Engineering*, 52(7):673–703, 2001.

[28] B. Wassermann, S. Kollmannsberger, T. Bog, and E. Rank. From geometric design to numerical analysis: A direct approach using the Finite Cell Method on Constructive Solid Geometry. *Computers and Mathematics with Applications*, 74(7): 1703–1726, 2017.

[29] M. Elhaddad, N. Zander, T. Bog, L. Kudela, S. Kollmannsberger, J. Kirschke, T. Baum, M. Ruess, and E. Rank. Multi-level *hp*-finite cell method for embedded interface problems with application in biomechanics. *International Journal for Numerical Methods in Biomedical Engineering*, 34(4), 2018.

[30] L. Kudela, S. Kollmannsberger, U. Almac, and E. Rank. Direct structural analysis of domains defined by point clouds. *Computer Methods in Applied Mechanics and Engineering*, 358, 2020.

[31] L. Kudela, N. Zander, S. Kollmannsberger, and E. Rank. Smart octrees: Accurately integrating discontinuous functions in 3D. *Computer Methods in Applied Mechanics and Engineering*, 306:406–426, 2016.

[32] S. Hubrich, P. Di Stolfo, L. Kudela, S. Kollmannsberger, E. Rank, A. Schröder, and A. Düster. Numerical integration of discontinuous functions: moment fitting and smart octree. *Computational Mechanics*, 60(5):863–881, 2017.

[33] M. Joulaian, S. Hubrich, and A. Düster. Numerical integration of discontinuities on arbitrary domains based on moment fitting. *Computational Mechanics*, 57(6): 979–999, 2016.

[34] A. Düster, J. Parvizian, Z. Yang, and E. Rank. The finite cell method for three-dimensional problems of solid mechanics. *Computer Methods in Applied Mechanics and Engineering*, 197(45-48):3768–3782, 2008.

[35] Z. Wassouf. *Die Mortar Methode für Finite Elemente hoher Ordnung*. PhD thesis, Technische Universität München, 2010.

[36] UNECE/FAO. *Forest Products Annual Market Review, 2019-2020*. United Nations, Geneva, 2020.

[37] E. Ussher and I. Smith. Predicting vibration behaviour of cross laminated timber floors. *IABSE Symposium Report*, 104(19):1–8, 2015.

[38] S. Mecking, T. Kruse, C. Winter, and U. Schanda. *Vibroakustik im Planungsprozess für Holzbauten – Modellierung, numerische Simulation, Validierung*. Schlussbericht zu IGF-Vorhaben Nr. 18724 N und 17328 N, Hochschule Rosenheim, 2017.

[39] Finnforest Merk GmbH. *Leno-Massivbau, LenoTec, Material + Konstruktion.* Aichach, 2004.

[40] Allgemeine bauaufsichtliche Zulassung Z-9.1-847: Furnierschichtholz "Kerto-S" und "Kerto-Q nach EN 14374". Deutsches Institut für Bautechnik, Berlin, Deutschland, 2014.

[41] K. Zaveri. *Modal Analysis of Large Structures – Multiple Exciter Systems.* Brüel & Kjær, Nærum, 1984.

[42] DIN EN 1912:2013-10: Bauholz für tragende Zwecke – Festigkeitsklassen – Zuordnung von visuellen Sortierklassen und Holzarten; Deutsche Fassung EN 1912:2012 + AC:2013. Beuth Verlag GmbH, Berlin, Deutschland, 2013.

[43] DIN EN 338:2016-07: Bauholz für tragende Zwecke – Festigkeitsklassen; Deutsche Fassung EN 338:2016. Beuth Verlag GmbH, Berlin, Deutschland, 2016.

[44] P. Niemz and D. Caduff. Untersuchungen zur Bestimmung der Poissonschen Konstanten an Fichtenholz. *Holz als Roh- und Werkstoff*, 66(1):1–4, 2008.

[45] R. J. Allemang and D. L. Brown. A correlation coefficient for modal vector analysis. 1:110–116, 1982.

[46] Getzner Werkstoffe GmbH. Data sheet of Sylodyn® ND. September 2014.

[47] DIN ISO 1827:2010-07: Elastomere oder thermoplastische Elastomere – Bestimmung des Schubmoduls und der Haftung zu starren Platten – Quadrupel-Schermethode (ISO 1827:2007). Beuth Verlag GmbH, Berlin, Deutschland, 2010.

[48] Getzner Werkstoffe GmbH. Data sheet of Sylodyn® NE. September 2014.

[49] A. Gülzow. *Zerstörungsfreie Bestimmung der Biegesteifigkeiten von Brettsperrholzplatten.* PhD thesis, Eidgenössische Technische Hochschule Zürich, 2008.

[50] A. Feldmann. *Dynamic Properties of Tall Timber Structures under Wind-indiced Vibration.* Master's thesis, Technische Universität München, 2015.

[51] T. Kruse. *Messung und Analyse des Schwingungsverhaltens von gekoppelten Bauteilen aus Brettsperrholz.* Master's thesis, Hochschule Rosenheim, 2016.

[52] J. Bodig and B.A. Jane. *Mechanics of Wood and Wood Composites.* Krieger Publishing Company, 1993.

[53] J. Eibl and U. Häussler-Combe. Baudynamik. *Beton-Kalender 1997, Teil 2*, pages 755–861.

[54] N. Labonnote, A. Rønnquist, B. Manum, and P. Rüther. Additive construction: State-of-the-art, challenges and opportunities. *Automation in Construction*, 72: 347–366, 2016.

[55] P. Wu, J. Wang, and X. Wang. A critical review of the use of 3-D printing in the construction industry. *Automation in Construction*, 68:21–31, 2016.

[56] D. Delgado Camacho, P. Clayton, W.J. O'Brien, C. Seepersad, M. Juenger, R. Ferron, and S. Salamone. Applications of additive manufacturing in the construction industry – A forward-looking review. *Automation in Construction*, 89:110–119, 2018.

[57] S.H. Ghaffar, J. Corker, and M. Fan. Additive manufacturing technology and its implementation in construction as an eco-innovative solution. *Automation in Construction*, 93:1–11, 2018.

[58] ISO/ASTM 52900:2015: Additive manufacturing – General principles – Terminology. International Organization for Standardization, Geneva, Switzerland, 2015.

[59] T.T. Le, S.A. Austin, S. Lim, R.A. Buswell, A.G.F. Gibb, and T. Thorpe. Mix design and fresh properties for high-performance printing concrete. *Materials and Structures/Materiaux et Constructions*, 45(8):1221–1232, 2012.

[60] R.A. Buswell, W.R. Leal de Silva, S.Z. Jones, and J. Dirrenberger. 3D printing using concrete extrusion: A roadmap for research. *Cement and Concrete Research*, 112:37–49, 2018.

[61] M. Näther, V.N. Nerella, M. Krause, G. Kunze, V. Mechtcherine, and R. Schach. *Beton-3D-Druck – Machbarkeitsuntersuchungen zu kontinuierlichen und schalungsfreien Bauverfahren durch 3D-Formung von Frischbeton. Abschlussbericht.* Forschungsinitiative Zukunft Bau, Band F 3024. Fraunhofer IRB Verlag, Stuttgart, 2017.

[62] T.A.M. Salet, F.P. Bos, R.J.M. Wolfs, and Z.Y. Ahmed. 3D concrete printing – A structural engineering perspective. In M. Lukovic and D.A. Hordijk, editors, *High Tech Concrete: Where Technology and Engineering Meet – Proceedings of the 2017 fib Symposium*, pages xliii–lvii. Springer International Publishing, 2017.

[63] F. Bos, R. Wolfs, Z. Ahmed, and T. Salet. Additive manufacturing of concrete in construction: potentials and challenges of 3D concrete printing. *Virtual and Physical Prototyping*, 11(3):209–225, 2016.

[64] T.A.M. Salet, Z.Y. Ahmed, F.P. Bos, and H.L.M. Laagland. Design of a 3D printed concrete bridge by testing. *Virtual and Physical Prototyping*, 13(3):222–236, 2018.

[65] D. Lowke, E. Dini, A. Perrot, D. Weger, C. Gehlen, and B. Dillenburger. Particle-bed 3D printing in concrete construction – Possibilities and challenges. *Cement and Concrete Research*, 112:50–65, 2018.

[66] Institute for Advanced Architecture of Catalonia (IAAC). 3D printed bridge. URL `https://iaac.net/project/3d-printed-bridge`. Accessed: April 22, 2021.

[67] V. Mechtcherine and V.N. Nerella. Incorporating reinforcement in 3D-printing with concrete [Integration der Bewehrung beim 3D-Druck mit Beton]. *Beton- und Stahlbetonbau*, 113(7):496–504, 2018.

[68] D. Asprone, C. Menna, F.P. Bos, T.A.M. Salet, J. Mata-Falcón, and W. Kaufmann. Rethinking reinforcement for digital fabrication with concrete. *Cement and Concrete Research*, 112:111–121, 2018.

[69] D. Herzog, V. Seyda, E. Wycisk, and C. Emmelmann. Additive manufacturing of metals. *Acta Materialia*, 117:371–392, 2016.

[70] W.E. Frazier. Metal additive manufacturing: A review. *Journal of Materials Engineering and Performance*, 23(6):1917–1928, 2014.

[71] C. Buchanan and L. Gardner. Metal 3D printing in construction: A review of methods, research, applications, opportunities and challenges. *Engineering Structures*, 180:332 – 348, 2019.

[72] T.D. Ngo, A. Kashani, G. Imbalzano, K.T.Q. Nguyen, and D. Hui. Additive manufacturing (3D printing): A review of materials, methods, applications and challenges. *Composites Part B: Engineering*, 143:172–196, 2018.

[73] S. Galjaard, S. Hofman, N. Perry, and S. Ren. Optimizing Structural Building Elements in Metal by using Additive Manufacturing. In *Proceedings of the IASS Annual Symposia*, 2015.

[74] D. Moreno Nieto, V. Casal López, and S.I. Molina. Large-format polymeric pellet-based additive manufacturing for the naval industry. *Additive Manufacturing*, 23: 79–85, 2018.

[75] Branch Technology. URL `https://www.branch.technology/`. Accessed: June 24, 2019.

[76] DUS Architects. KamerMaker. URL `http://3dprintcanalhouse.com/`. Accessed: June 24, 2019.

[77] C.E. Duty, V. Kunc, B. Compton, B. Post, D. Erdman, R. Smith, R. Lind, P. Lloyd, and L. Love. Structure and mechanical behavior of Big Area Additive Manufacturing (BAAM) materials. *Rapid Prototyping Journal*, 23(1):181–189, 2017.

[78] K. Biswas, J. Rose, L. Eikevik, M. Guerguis, P. Enquist, B. Lee, L. Love, J. Green, and R. Jackson. Additive Manufacturing Integrated Energy-Enabling Innovative Solutions for Buildings of the Future. *Journal of Solar Energy Engineering, Transactions of the ASME*, 139(1), 2017.

[79] 3D Systems. 3D Printing Hits New Heights in Architecture. URL `https://www.3dsystems.com/blog/2013/09/3d-printing-hits-new-heights-architecture`. Accessed: June 24, 2019.

[80] Skanska. 3D printing for construction. URL `https://www.skanska.co.uk/about-skanska/innovation-and-digital-engineering/innovation/3d-printing`. Accessed: June 24, 2019.

[81] P. Parandoush and D. Lin. A review on additive manufacturing of polymer-fiber composites. *Composite Structures*, 182:36–53, 2017.

[82] O. Sigmund and K. Maute. Topology optimization approaches: A comparative review. *Structural and Multidisciplinary Optimization*, 48(6):1031–1055, 2013.

[83] J. Liu, A.T. Gaynor, S. Chen, Z. Kang, K. Suresh, A. Takezawa, L. Li, J. Kato, J. Tang, C.C.L. Wang, L. Cheng, X. Liang, and A.C. To. Current and future trends in topology optimization for additive manufacturing. *Structural and Multidisciplinary Optimization*, 57(6):2457–2483, 2018.

[84] M.K. Thompson, G. Moroni, T. Vaneker, G. Fadel, R.I. Campbell, I. Gibson, A. Bernard, J. Schulz, P. Graf, B. Ahuja, and F. Martina. Design for Additive Manufacturing: Trends, opportunities, considerations, and constraints. *CIRP Annals - Manufacturing Technology*, 65(2):737–760, 2016.

[85] M. Livesu, S. Ellero, J. Martínez, S. Lefebvre, and M. Attene. From 3D models to 3D prints: an overview of the processing pipeline. *Computer Graphics Forum*, 36 (2):537–564, 2017.

[86] R.R. Lipman and J.S. McFarlane. Exploring Model-Based Engineering Concepts for Additive Manufacturing. In *Proceedings of the 26th Solid Freeform Fabrication Symposium*, Austin, Texas, 2015.

[87] ISO 16739-1:2018: Industry Foundation Classes (IFC) for data sharing in the construction and facility management industries – Part 1: Data schema. International Organization for Standardization, Geneva, Switzerland, 2018.

[88] A. Borrmann, M. König, C. Koch, and J. Beetz, editors. *Building Information Modeling – Technology Foundations and Industry Practice*. Springer, Cham, 2018.

[89] G. Savio, S. Rosso, R. Meneghello, and G. Concheri. Geometric modeling of cellular materials for additive manufacturing in biomedical field: A review. *Applied Bionics and Biomechanics*, 2018.

[90] G. Savio, R. Meneghello, and G. Concheri. Geometric modeling of lattice structures for additive manufacturing. *Rapid Prototyping Journal*, 24(2):351–360, 2018.

[91] F. Tamburrino, S. Graziosi, and M. Bordegoni. The design process of additively manufactured mesoscale lattice structures: A review. *Journal of Computing and Information Science in Engineering*, 18(4), 2018.

[92] X.Y. Kou and S.T. Tan. Heterogeneous object modeling: A review. *CAD Computer Aided Design*, 39(4):284–301, 2007.

[93] F. Massarwi and G. Elber. A B-spline based framework for volumetric object modeling. *CAD Computer Aided Design*, 78:36–47, 2016.

[94] T. Dokken, V. Skytt, and O. Barrowclough. Trivariate spline representations for computer aided design and additive manufacturing. *Computers and Mathematics with Applications*, 2018.

[95] O. Davtalab, A. Kazemian, and B. Khoshnevis. Perspectives on a BIM-integrated software platform for robotic construction through Contour Crafting. *Automation in Construction*, 89:13–23, 2018.

[96] R.J.M. Wolfs, F.P. Bos, and T.A.M. Salet. Early age mechanical behaviour of 3D printed concrete: Numerical modelling and experimental testing. *Cement and Concrete Research*, 106:103–116, 2018.

[97] R.J.M. Wolfs, F.P. Bos, and T.A.M. Salet. Triaxial compression testing on early age concrete for numerical analysis of 3D concrete printing. *Cement and Concrete Composites*, 104, 2019.

[98] M. Megahed, H.W. Mindt, N. N'Dri, H. Duan, and O. Desmaison. Metal additive-manufacturing process and residual stress modeling. *Integrating Materials and Manufacturing Innovation*, 5(1):61–93, Dec 2016.

[99] M. Chiumenti, X. Lin, M. Cervera, W. Lei, Y. Zheng, and W. Huang. Numerical simulation and experimental calibration of additive manufacturing by blown powder technology. Part I: Thermal analysis. *Rapid Prototyping Journal*, 23(2):448–463, 2017.

[100] J. Lindwall, A. Malmelöv, A. Lundbäck, and L.-E. Lindgren. Efficiency and Accuracy in Thermal Simulation of Powder Bed Fusion of Bulk Metallic Glass. *JOM*, 70 (8):1598–1603, 2018.

[101] E. Neiva, S. Badia, A.F. Martín, and M. Chiumenti. A scalable parallel finite element framework for growing geometries. Application to metal additive manufacturing. *International Journal for Numerical Methods in Engineering*, pages 1–28, 2019.

[102] S. Jayanath and A. Achuthan. A Computationally Efficient Finite Element Framework to Simulate Additive Manufacturing Processes. *Journal of Manufacturing Science and Engineering, Transactions of the ASME*, 140(4), 2018.

[103] S. Kollmannsberger, A. Özcan, M. Carraturo, N. Zander, and E. Rank. A hierarchical computational model for moving thermal loads and phase changes with applications to selective laser melting. *Computers and Mathematics with Applications*, 75(5):1483–1497, 2018.

[104] M.R. Talagani, S. Dormohammadi, R. Dutton, C. Godines, H. Baid, F. Abdi, V. Kunc, B. Compton, S. Simunovic, C. Duty, L. Love, B. Post, and C. Blue. Numerical simulation of big area additive manufacturing (3D printing) of a full size car. *SAMPE Journal*, 51(4):27–36, 2015.

[105] B. Brenken, E. Barocio, A. Favaloro, V. Kunc, and R.B. Pipes. Development and validation of extrusion deposition additive manufacturing process simulations. *Additive Manufacturing*, 25:218–226, 2019.

[106] A. Cattenone, S. Morganti, G. Alaimo, and F. Auricchio. Finite element analysis of additive manufacturing based on fused deposition modeling: Distortions prediction and comparison with experimental data. *Journal of Manufacturing Science and Engineering, Transactions of the ASME*, 141(1), 2019.

[107] M. Ganci, W. Zhu, G. Buffa, L. Fratini, S. Bo, and C. Yan. A macroscale FEM-based approach for selective laser sintering of thermoplastics. *International Journal of Advanced Manufacturing Technology*, 91(9-12):3169–3180, 2017.

[108] A. Amado, M. Schmid, and K. Wegener. Simulation of warpage induced by non-isothermal crystallization of co-polypropylene during the SLS process. In *AIP Conference Proceedings*, 2015.

[109] D. Riedlbauer, P. Steinmann, and J. Mergheim. Thermomechanical simulation of the selective laser melting process for PA12 including volumetric shrinkage. In *AIP Conference Proceedings*, 2015.

[110] W. Yan, S. Lin, O.L. Kafka, C. Yu, Z. Liu, Y. Lian, S. Wolff, J. Cao, G.J. Wagner, and W.K. Liu. Modeling process-structure-property relationships for additive manufacturing. *Frontiers of Mechanical Engineering*, 13(4):482–492, 2018.

[111] T.T. Le, S.A. Austin, S. Lim, R.A. Buswell, R. Law, A.G.F. Gibb, and T. Thorpe. Hardened properties of high-performance printing concrete. *Cement and Concrete Research*, 42(3):558–566, 2012.

[112] B. Zareiyan and B. Khoshnevis. Interlayer adhesion and strength of structures in Contour Crafting – Effects of aggregate size, extrusion rate, and layer thickness. *Automation in Construction*, 81:112–121, 2017.

[113] B. Zareiyan and B. Khoshnevis. Effects of interlocking on interlayer adhesion and strength of structures in 3D printing of concrete. *Automation in Construction*, 83: 212–221, 2017.

[114] B. Zareiyan and B. Khoshnevis. Effects of mixture ingredients on interlayer adhesion of concrete in Contour Crafting. *Rapid Prototyping Journal*, 24(3):584–592, 2018.

[115] V.N. Nerella, S. Hempel, and V. Mechtcherine. Effects of layer-interface properties on mechanical performance of concrete elements produced by extrusion-based 3D-printing. *Construction and Building Materials*, 205:586–601, 2019.

[116] R.J.M. Wolfs, F.P. Bos, and T.A.M. Salet. Hardened properties of 3D printed concrete: The influence of process parameters on interlayer adhesion. *Cement and Concrete Research*, 119:132–140, 2019.

[117] C. Buchanan, V.-P. Matilainen, A. Salminen, and L. Gardner. Structural performance of additive manufactured metallic material and cross-sections. *Journal of Constructional Steel Research*, 136:35–48, 2017.

[118] S. Joosten. Printing a stainless steel bridge. Master's thesis, Delft University of Technology, Delft, Netherlands, 2015. Accessed: June 24, 2019.

[119] F.P. Bos, E. Bosco, and T.A.M. Salet. Ductility of 3D printed concrete reinforced with short straight steel fibers. *Virtual and Physical Prototyping*, pages 1–15. Published online: November 19, 2018.

[120] N. Korshunova, G. Alaimo, S.B. Hosseini, M. Carraturo, A. Reali, J. Niiranen, F. Auricchio, E. Rank, and S. Kollmannsberger. Image-based numerical characterization and experimental validation of tensile behavior of octet-truss lattice structures. *Additive Manufacturing*, 41, 2021.

[121] M. Carraturo, G. Alaimo, S. Marconi, E. Negrello, E. Sgambitterra, C. Maletta, A. Reali, and F. Auricchio. Experimental and Numerical Evaluation of Mechanical Properties of 3D-Printed Stainless Steel 316L Lattice Structures. *Journal of Materials Engineering and Performance*, 2021.

[122] A. Ferrigno, F. Di Caprio, R. Borrelli, F. Auricchio, and A. Vigliotti. The mechanical strength of Ti-6Al-4V columns with regular octet microstructure manufactured by electron beam melting. *Materialia*, 5, 2019.

[123] R. Hedayati, H. Hosseini-Toudeshky, M. Sadighi, M. Mohammadi-Aghdam, and A.A. Zadpoor. Computational prediction of the fatigue behavior of additively manufactured porous metallic biomaterials. *International Journal of Fatigue*, 84:67–79, 2016.

[124] M. Domingo-Espin, J.M. Puigoriol-Forcada, A.-A. Garcia-Granada, J. Llumà, S. Borros, and G. Reyes. Mechanical property characterization and simulation of fused deposition modeling Polycarbonate parts. *Materials and Design*, 83:670–677, 2015.

[125] M. Ashraf, I. Gibson, and M.G. Rashed. Challenges and prospects of 3d printing in structural engineering. In *Proceedings of the 13th International Conference on Steel, Space and Composite Structures*, Perth, Australia, 2018.

[126] Å. Bolmsvik and A. Brandt. Damping assessment of light wooden assembly with and without damping material. *Engineering Structures*, 49:434–447, 2013.

[127] L.S. Cook and R.S. Lakes. Damping at high homologous temperature in pure Cd, In, Pb, and Sn. *Scripta Metallurgica et Materiala*, 32(5):773–777, 1995.

[128] S.P. Balch and R.S. Lakes. High vibration damping in in situ In-Zn composites. *Functional Materials Letters*, 8(5), 2015.

[129] H. Lu, X. Wang, T. Zhang, Z. Cheng, and Q. Fang. Design, fabrication, and properties of high damping metal matrix composites – A review. *Materials*, 2(3): 958–977, 2009.

[130] D. Siva Prasad and C. Shoba. Damping Behavior of Metal Matrix Composites. *Transactions of the Indian Institute of Metals*, 68(2):161–167, 2015.

[131] L. Salari-Sharif, T.A. Schaedler, and L. Valdevit. Hybrid Hollow Microlattices with Unique Combination of Stiffness and Damping. *Journal of Engineering Materials and Technology, Transactions of the ASME*, 140(3), 2018.

[132] R. Casati, J. Lemke, and M. Vedani. Microstructure and Fracture Behavior of 316L Austenitic Stainless Steel Produced by Selective Laser Melting. *Journal of Materials Science and Technology*, 32(8):738–744, 2016.

[133] EOS GmbH. Material data sheet of EOS StainlessSteel 316L. June 2014.

[134] S.S. Jung, Y.T. Kim, Y.B. Lee, S.H. Shin, D. Kim, and H.C. Kim. Measurement of the resonance frequency, the loss factor, and the dynamic Young's modulus in structural steel and polycarbonate by using an acoustic velocity sensor. *Journal of the Korean Physical Society*, 49(5):1961–1966, 2006.

[135] S.S. Jung, B.S. Jeon, J. Jin, and Y.B. Lee. Measurement of the loss factor and the Young's modulus in acrylonitrile butadiene styrene and Polymethyl Methacrylate by using an acoustic wave generator. *International Journal of Precision Engineering and Manufacturing*, 15(12):2493–2497, 2014.

[136] S.S. Jung, Y.B. Lee, B.S. Jeon, and S.H. Shin. Measurement of the loss factor and the Young's modulus in structural steel by using a laser beam reflection method. *Journal of the Korean Physical Society*, 65(7):1024–1027, 2014.

[137] S.H. Shin, Y.B. Lee, S.S. Jung, and D.H. Lee. Determination of the Young's modulus and loss factor by acoustic bending vibration methods. *Key Engineering Materials*, 297-300 III:1958–1961, 2005.

[138] S. Corn, J.-S. Dupuy, P. Ienny, and L. Daridon. Vibration analysis techniques for detecting filler-matrix decohesion in composites. *Revue des Composites et des Materiaux Avances*, 22(1):77–90, 2012.

[139] W. Fu and D.D.L. Chung. Vibration reduction ability of polymers, particularly polymethylmethacrylate and polytetrafluoroethylene. *Polymers and Polymer Composites*, 9(6):423–426, 2001.

[140] N. Korshunova, J. Jomo, G. Lékó, D. Reznik, P. Balázs, and S. Kollmannsberger. Image-based material characterization of complex microarchitectured additively manufactured structures. *Computers and Mathematics with Applications*, 80(11): 2462–2480, 2020.